Energy dissipation in a simulated fault system

by
Munib Sarwar
Physics of Geological Processes
Department of Physics
University of Oslo
Norway

Thesis submitted for the degree
Master of Science

October 2008

Abstract

The energy dissipation in an earthquake can be partitioned into three components $W_{tot} = W_{radiated} + W_{expansion} + W_{friction}$, where $W_{radiated}$ is the seismic radiated energy, $W_{expansion}$ is the energy consumed propogating the fault and producing new surfaces, and $W_{friction}$ is the energy used to resist the frictional strength of the fault. Characterizing each of these components in order to estimate this total energy budget and the energy dissipated during fault dynamics is essential for getting a better understanding of earthquake physics. Even though there have been great advancements in the physics of earthquakes in the recent decades there is still not complete agreement on the role of the different energy components. In this thesis we simulate a fault system by sliding an indenter (glass bead) across the surface of a halite crystal. Since halite is transparent in the mid infrared range $\Delta\lambda = 3 - 5\mu m$ we can monitor the radiation emission at the sliding surface (coated with black anti-reflective paint) through the crystal with an infrared camera and quantify the temperature increase caused by the frictional sliding at the surface. Using an analytical model describing the thermal diffusion of a 2D point heat source inside the crystal we estimate the thermal energy generated in the frictional sliding experiment from the temperature data acquired with the infrared camera. From this analysis we get that the energy dissipated in heat is 26% of the total work applied in the experiment. Analysing the surface of the crystal after a frictional sliding experiment we observe a breakage pattern inside the groove, and from this pattern we estimate an upper limit of the energy spent creating new surfaces in the plastically deformed region of the crystal. The upper estimation we get for the energy spent creating new surfaces in an experiment is 12% of the total work applied during sliding. The contribution from the friction of the rig and the acoustic emission could not yet be estimated.

Acknowledgement

I want to start out by thanking my supervisors Karen Mair and Dag Kristhian Dysthe for the guidance that they have given me and for helping me face all the challenges in the project, your opinions and views have been invaluable to me.

I also want to thank Stephane Santucci who have been both a guide and a colleague, for his great ideas and numerous discussions. A man that can not be fortgotten is Olav Gundersen, who I want to thank for all the technical help throughout the project. I would also like to thank Karen Mair and Francois Renard for starting this interesting project.

The master students at PGP I thank you for your company and friendship, it has been an amazing journey where I have learnt just as much from you as anybody else. All the PHD students and postdoc. students you are an inspiaration and give me courage to work even harder. I would like to thank Filip, Marcin, Cristoph and Victoria for their help in making me understand my project better.

Especially I would like to than Yuri Podladchikov for all the help he has given me, and for teaching me knew ways of solving problems in physics.

At the end I will like to thanks all the people at PGP and physics department for som very interesting years.

Contents

Chapter 1

Introduction and Motivation

Movement of the earths crust builds up stresses in a fault zone, and when these stresses reach a critical point we get slippage along the fault planes that cause earthquakes. The energy dissipated in an earthquake is in plate tectonic physics partitioned into three different components

$$W_{tot} = W_{radiated} + W_{expansion} + W_{friction},$$

where W_{tot} is the total work. The first component on the right hand side is the energy radiated in seismic waves and the only part of the energy budget that can be measured in the field while the earthquake is happening. Even with recent advances in seismology there is still not complete agreement on the best technique to measure and estimate radiated energy (*Venkataraman et. al* [34]). The second term in the equation comes from expanding fractures and generating new surface area in the fault zone. This component is estimated using Griffiths energy balance relation between the energy needed to for the crack to grow and the work that needs to be applied to generate new surface area [1]. The deformation in a fault zone, according to Scholz [1] happens not only at the cracktips, but also as micro cracks behind it in a brittle process zone along the fault plane. These micro cracks combine themselves as the crack advances to a macroscopic fracture. The total work needed to expand the fault $W_{expansion}$ is then calculated with all of this surface taken into account. The third component $W_{friction}$ in the energy budget is the work done to overcome frictional strength of the fault. The energy used to overcome the fault strength is assumed to be completely dissipated in heat in tectonical physics, e.g. *Kanamori and Rivera* [17], *M. L. Cooke and Susan Murphy* [6] and *Michael L. Blanpied et.al.* [23]. Estimating the frictional work is not possible from seismological data alone, since there are no methods on estimating the absolute level of stress on the fault (*Kanamori and Rivera* [17]).

Knowing how these components make up the total energy budget is essential for having a good understanding of the physics of earthquakes. Despite the recent advancements in seismic instrumentation and computational facility, there is still wide disagreement on the role of different energy components in earthquake physics, *Hiroo Kanamori* [16]. The quantitative estimation of these components vary depending on what method is applied.

1.1 Heating as a slip weakening mechanism

Consider a fault plane under the stress σ_I initially, then there is a sudden increase of the stress to the critical level σ_y resulting in yielding of the fault and slippage along the fault plane. The stress than decreases to σ_F during slip D_c and remains there for rest of the slip motion to D. This model is called the slip weakening model and a graphic description of it is given in figure 1.1. Energy dissipated while decreasing the stress to σ_F is assumed to

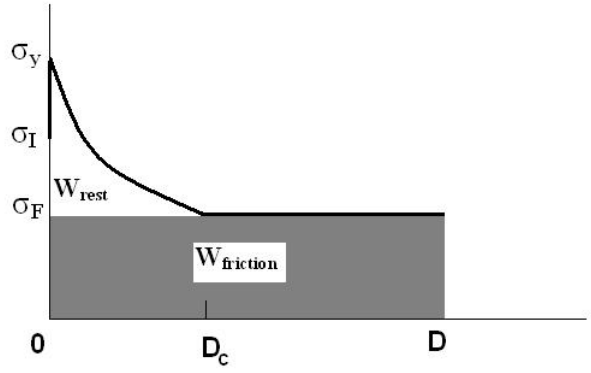

Figure 1.1: A simple graphic description of the slip weakening model. The stress on the fault plain rises from σ_I to yield stress σ_y causing slip. The stress so decreases to σ_F needed to sustain the slip to distance D. Energy in the gray area is the frictional energy and the rest is the propagated and surface energy (given in unit per area).

consist of seismic radiated energy and energy needed to generate new surface area. Rest of the energy marked gray is all dissipated as frictional work.

One weakening mechanism in mature faults that has been extensively studied is the response of fluid pressure to frictional heating (*Sibson* [30], *Lachenbruch* [19], *Mase and Smith* [21], [22]). These studies investigate how the permeability, the width of the shear zone, initial stress, and factors con-

trolling transient hydrofracture and pore dilation. Mase and Smith investigated the effect of these parameters using numerical modelling technique in their 1985 paper [21]. They showed that the response of fluid pressures to frictional heating could be described by two limiting cases. If the permeability or compressibility of the porous medium exceeds the values $10^{-15}\mathrm{m}^2$ or $10^{-8}\mathrm{Pa}^{-1}$, then the thermal expansion of pore fluid is accommodated by fluid flow from or pore dilation within the heated region adjacent to the fault surface. Resulting the fault acts as a strong frictional heat source. If the permeability or compressibility of the porous medium are below the values $10^{-19}\mathrm{m}^2$ and $10^{-11}\mathrm{Pa}^{-1}$, then the heating process takes place at constant fluid mass, and substantial increase in fluid pressure can occur. This diminishes the shear strength rapidly to a value sufficient to maintain the thermal pressurization process, and in this case the temperature will be less than that required for melting.

Newer studies of shear localization along a fault zone, suggest a much narrower principal slip surface than what was previously widely accepted, *Chester and Chester* [5], *Sibson* [31], *Noda and Shimamoto* [24]. Newer models have been developed to investigate the effect of frictional heating and thermal expansion under these conditions, *Rempel and Rice* [25], *Bizzari and Cocco* [2] and *Rice* [26]. Trying to analyse the weakening mechanisms in such narrow faults Rice developed analytical models describing two different mechanisms that could lead to thermal weakening. One of the weakening mechanisms considered by Rice is the thermal pressurization of pore fluid within the fault zone by frictional heating. The other process is flash weakening that happens by contact of micron scale asperities during rapid slippage. These micron contacts are subjected to very large stresses and produce high temperatures, referred to as flash heat, consequently decreasing the friction coefficient and the frictional strength. This process has previously been analysed in tribology physics when looking at high speed frictional response of metals, e.g. Bowden and Thomas [3]. Another weakening mechanism that is considered to be important is the creation silica gel, which is observed in experiments that include high slip rate and confining stresses such as *Goldsby and Tullis* [10] and *Di Toro et.al.* [8]. In conditions where there is large initial effective stress and slip, melting might occur along the fault surface, this melt will then, if it is hot and have low enough viscosity, lubricate the fault reducing dynamic friction. The complex behaviour of this process has been studied by *Sibson* [29], *Tsatsumi and Shimamoto* [33], *Hirose and Shimamoto* [11], and *Brodsky and Kanamori* [4].

1.2 The frictional sliding experiments

The aim of Our project is to analyse the energy partitioning during frictional sliding on a simulated fault system, in order to increase the understanding of how energy dissipation relates to earthquake weakening mechanisms. We simulate a fault in the laboratory by dragging sandpaper across a halite crystal, which is held under constant normal load. During sliding we measure the vertical displacement of the crystal, the horizontal displacement of the sandpaper and the shear force applied dragging the sandpaper. Since halite has a high transmissivity in the infrared region we can look through it and monitor the radiation changes because of heat generation using an infrared camera at the sliding surface. The contact between the sandpaper and the crystal happens only at some few sand grains, these sand grains dig into the crystal and create scratches.

This experimental method was developed by *K. Mair* and *F. Renard* to investigate the mechanics of earthquakes and how heat is dissipated in frictional sliding. The work so far has been focused on thermal dissipation and trying to analyse the amount of energy that is dissipated as thermal energy [20]. The frictional response has been so far mainly been explored for three different sliding velocities (v =0.6, 0.9, 1.7mm/s) and three different surface conditions bare cleaved halite surface over sandpaper, rough halite surface over sandpaper and sand gouge between sandpaper an rough halite surface. In the paper they describe how the friction coefficient μ (shear stress/normal load) peaks shortly after sliding starts, and right afterwards stabilizes on a relative steady friction value. For coarse sandpaper the friction stabilizes at about $\mu = 1$ and in the case of having a gouge layer the friction stabilizes at about $\mu = 0.6$. The radiation profile is monitored at the sliding interface using an infrared camera. For the bare surface they find a monotonic increase in average temperature and in the case of gouge layer a rapid initial increase is observed that slows down and reaches a steady state after about 5-10sec. For the bare surface the radiation profile is observed to be highly heterogeneous and with localization of high radiation emission at contact points between the sand grains of the sandpaper and the crystal.

1.2.1 The experiments presented in this thesis

The experiments and research we have done during the master thesis is a continuation of *K. Mair* and *F. Renards* work [20]. The experimental setup is the same as have been used by them, described above. To make it easier to quantify the thermal radiation signal from the radiation signal change that happens because of wear we will try to improve the measuring tech-

nique. Since a lot of scratches are created simultaneously in the sandpaper experiments we will change the sandpaper to a single indenter scratching the crystal. This will make it easier to connect the heat dissipation and the deformation energy spent directly to one single groove. This single indenter experiments are known in the tribology science as scratch test and used for determining the hardness properties of materials.

I will start out with going through the black body radiation theory in chapter 2. Understanding of the radiation emission from an object is essential to understand what one measures with an infrared camera and how it relates to temperature changes. The explanation given in this chapter will be used throughout the thesis when analysing the thermal radiation signals in the experiments and when calibrating the infrared camera to different setups.

In Chapter 3 we look into how the infrared camera works and explain some features of the particular camera that one has to be aware of when using it. How well the internal cooling of the IR camera effects the calibration result, which determines to what accuracy one is able predict the thermal increase in the experiments. We also explore a calibration technique with a peltier element and look into how well the radiation signal change measured compares to the theoretical radiation change of a blackbody (a perfect emitter).

In chapter 4 we do a rough calibration of the infrared camera to a halite crystal laying on a sandpaper. Therafter we investigate how the emissivity changes because of wear affects the radiation signal. In an attempt to distinguish the thermal radiation signal from the radiation signal that happens because of emissivity changes we paint the crystal with anti-reflective coating, which blocks out the background and creates a temperature indicator layer on the sliding surface. In order to compare the radiation changes monitored in the experiment with real temperature signal we manually heat up the crystal and watch it diffuse. Even with all of these attempts to analyse the thermal dissipation we am not able to identify the radiation signal change caused by heat production.

In chapter 5 experiments using a single indenter in the form of a small glass bead are presented. This not only helps on connecting the mechanical data directly to the scratch, but also makes it easier to analyse the thermal dissipation. Painting the crystal with anti-reflective coating we observe radiation signals on the painted surface and are able to interpret them into temperature. We also observe a temperature increase with a thermistor during scratching that is attached to the crystal edge.

In chapter 6 we analyse the radiation signal observed in the single indenter experiments. Linking the radiation signal with thermal changes on the sliding surface we try to find out what the total increase in thermal energy was in the

experiments. First we compare the measurements with an one dimensional source point solution, thereafter we compare it to a two dimensional source point solution.

In chapter 7 we investigate the surface topography of the Halite crystal, after deformation, with a white light interferometer. Using this surface profile we analyse the deformation pattern inside and outside of the groove. From looking at the surface profile result we make some assumption that simplifies the breakage pattern observed and predict the amount of energy consumed at creating new surface area in the halite.

Chapter 2

Theory

2.1 Blackbody radiation

All matter continuously emits and absorbs electromagnetic radiation. An ideal surface that is capable of totally absorbing all incident radiation at any wavelength is defined as a blackbody. A blackbody is also then a perfect emitter since for any object to maintain thermal equilibrium with the surroundings it must emit the same amount of radiation it absorbs (Kirchoff's law). The theory of blackbody radiation can best be understood by the classical example of the radiation emitted from a small hole entrance of a cavity, dimensions of which are large in comparison to the hole. Radiation entering the hole would reflect inside the cavity, getting some amount absorbed each time, with very small possibility of ever escaping. Since the interior walls are considered to be in thermal equilibrium with each other, the radiation would continually be emitted and reabsorbed inside the box. The radiation that finally is emitted from the entrance hole of the cavity to the outside would be continuously distributed in all wavelengths.

Deriving an empirical law describing the energy and frequency measured from such an object was a major challenge in theoretical physics in late nineteenth century (first posed by Kirchoff in 1859). In one attempt to solve this problem the English physicist Lord Rayleigh considered the radiation inside the box to be a collection of standing waves in a cubical enclosure: electromagnetic oscillators. Further he assumed that the distribution of energy was determined by the equipartition theorem from which it follows that the average electromagnetic standing wave has the energy kT, where k is the Boltzmann's constant. Thus he came to the result for the spectral radiance emitted by a blackbody known as the Rayleigh-Jeans law

$$I(\lambda, T) = \frac{2\pi ckT}{\lambda}. \tag{2.1}$$

At large wavelengths this equation agrees well with the experimentally measured emittance from a blackbody, but as we approach smaller wavelengths (near ultraviolet) it diverges from the experimental result. The experimentally measured radiance goes to zero for smaller wavelengths while the Rayleigh-Jeans law diverges to infinity (see figure 2.1). This disagreement between theory and experiments was named the *Ultraviolet catastrophe* by Ehrenfest.

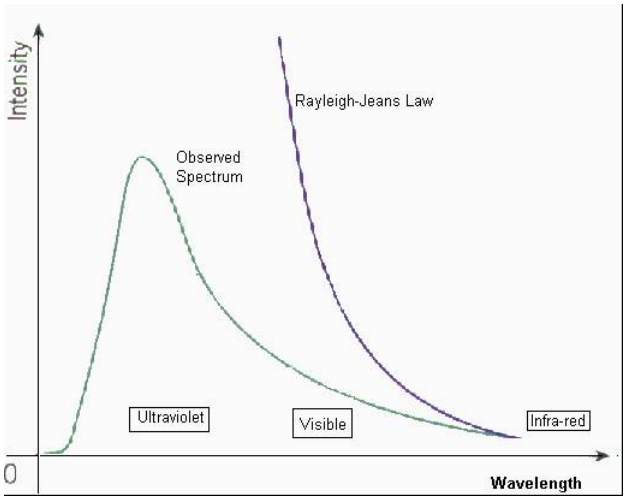

Figure 2.1: Curves showing the prediction made by Rayleigh-Jeans law and the experimentally observed radiation spectrum. The deviation of these curves as the wavelength approaches zero is called the ultraviolet catastrophe. The plot is taken from www.egglescliffe.org.uk [15]

At last it was the German physicist Karl Ernst Ludwig Marx Planck who solved this problem in 1900. Planck assumed that electromagnetic oscillators (electrons) inside the box could only have certain quanta sized energies with the value nhf, where f is the frequency, n=0,1,2... and h is Plancks constant. The final equation for the spectral radiance emitted by a blackbody he derived from these assumption is known as Planck's radiation law

$$I(\lambda, T) = \frac{2\pi hc^2}{\lambda^5 \left(e^{\frac{hc}{\lambda kT}} - 1 \right)}, \tag{2.2}$$

with the units energy per unit surface area, per unit time, per unit wavelength $[\frac{J}{m^3 s}]$. The derivation of Plancks radiation law is given in numerous thermal physics books, one such is Daniel V. Schroeders *Thermal Physics* [28]. This solution led further to what is called the birth of quantum mechanics.

2.2 Grey body

A real material does not behave like a blackbody it only emits a fraction of the radiation predicted by Plancks law. The fraction emitted ε of the incidented radiation is called the emissivity. A real object exposed to a certain amount of radiation will absorb a fraction α, reflect a fraction r and transmit a fraction τ. From conservation of energy these fractions must sum up to

$$\tau + \alpha + r = 1. \tag{2.3}$$

If the material is in thermal equilibrium it must emit the same amount of radiation it absorbs

$$\alpha = \varepsilon, \tag{2.4}$$

known as Kirchoffs law. The total amount of radiation energy emitted by a real object for a given temperature is

$$R\left(T\right) = \varepsilon \int_0^\infty I_{\lambda b}\left(\lambda, T\right) d\lambda = \varepsilon \int_0^\infty \frac{2\pi hc^2}{\lambda^5 \left(e^{\frac{hc}{\lambda kT}} - 1\right)} d\lambda, \tag{2.5}$$

where $I_b\left(\lambda, T\right)$ is the spectral intensity of a black body. In this equation we use us the total emissivity which is averaged over all its variables. In practical applications though the emissivity can depend on several variables such as the wavelength, the temperature of the emitter and angle of emission. The most fundamental expression of emissivity, with all variables taken into account, is $\varepsilon\left(\lambda, \theta, \phi, T\right)$ called the directional spectral emissivity, where θ and ϕ are the angles in a spherical coordinate system. If we average over all wavelengths we get the directional total emissivity $\varepsilon\left(\theta, \phi, T\right)$, and averaging over all directions gives the hemispherical spectral emissivity $\varepsilon\left(\lambda, T\right)$. A very neat mathematical description of the radiation properties of real objects is given in the book *Thermal radiation heat transfer* by Robert S. and John H. [32]. When working with an infrared camera we always look normally on the surface and within a given waveband $\Delta\lambda$. The emissivity we are subjected to in the experiments is then averaged over a given solid angle and a given waveband

$$\varepsilon_{\Delta\lambda,\theta,\varphi}\left(T\right) = \frac{\int_\varphi \int_\theta \int_{\Delta\lambda} \varepsilon\left(\lambda, \theta, \phi, T\right) I_{\lambda b}\left(\lambda, T\right) cos\theta sin\theta d\lambda d\theta d\phi}{\int_{\Delta\lambda} I_{\lambda b}\left(\lambda, T\right) d\lambda}, \tag{2.6}$$

where $\cos\theta$ comes from *Lambert's cosine law* [32]. Since we will always use the infrared camera in a small temperature range we can assume that the

emissivity is constant with regard to temperature differences. The radiation energy monitored by the infrared camera is than

$$R\left(T\right)=\varepsilon_{\Delta\lambda,\theta,\varphi,T}\int_{\Delta\lambda}I_{\lambda b}\left(\lambda,T\right)d\lambda \tag{2.7}$$

with the units energy per unit surface area, per unit time $[\frac{J}{m^2 s}]$. Further in the thesis R will be referred to as the radiant excitance and I as the intensity.

Chapter 3

The Infrared camera

The thermal energy dissipated in an experiment is monitored with the infrared camera Indigo Phoenix. The camera is sensitive in the mid-infrared region with a cold filter bandpass for 3-5μm, with a resolution of 256×320 pixels. The field of view with the optics used in all the experiments and calibrations is 8×10mm. In this chapter we will go through the method of calibration of the camera and different sources of errors that can modify the measurements. To be able to characterize the behaviour of the infrared camera we must have a temperature controller; for this, we will use a peltier element.

3.1 Material properties of sodium chloride

In all the experiments in this thesis we monitor the radiation signal with an infrared camera at the sliding surface looking through a halite crystal. Halite is highly transmissive in the infrared range with a transmittance up to 92%, a graph showing the transmittance of sodium chloride is given in appendix A [1]. The specific heat capacity of halite and the thermal consuctivity are $C_p = 854[J/kg \cdot K]$ and $\lambda = 1.15W/m \cdot K$ [14], and the density is 2.1-2.6·$10^3 kg/m^3$ [13], a datasheet on the material properties can be found at [14].

3.2 PID controller

The infrared camera will be calibrated by using a peltier element. A peltier element consists of n- and p- semiconductors arranged in pairs between two

[1] The graph is taken from the company Crystran Ltd, the suppliers of the crystal [14]

metal plates, and giving a current through these conducters produces a temperature difference between the two surfaces of the peltier element. To get consistent and replicable measurements by the IR camera we have to control the voltage sent into the peltier element to stabilize it on a given temperature (set point T_0). This can be done by a feedback loop were we take a reading from a thermistor and send out voltage according to the difference between the current temperature and the set point (error e). The algorithm we use to do this consist of a PID controller, which stands for Partial, Integral and Derivative controller. A PID controller uses the equation

$$V_{out} = P_{out} + I_{out} + D_{out}, \tag{3.1}$$

for the output signal. The different parts are estimated by:

$$\begin{aligned} P_{out} &= KP \cdot e, \\ I_{out} &= \int_0^t KI \cdot e \cdot d\tau, \\ D_{out} &= KD\frac{de}{dt}, \end{aligned}$$

e is the error and KP, KI and KD are the tuning parameters called proportional-, integral- and derivative gain. This PID controller program has been built in Labview and can control the temperature of the peltier element surface down to 2mK (the program is given in appendix B).

To get rid of reflections and impurities on the surface of the peltier element we coated it with black anti-reflective paint. This brought down the standard deviation of the picture taken by the IR camera to less than 6S. Even after this anti-reflective coating we see some pattern that remains in the IR signals that must be because of the optics or a small amount of reflection of the optics. Now that the peltier element has been coated with anti reflective coating, we can analyse the behaviour of the IR camera while looking at a surface at stable temperature.

3.3 Gradient in the IR camera image

One characteristic that on has to be aware of while working with the IR camera is that there is gradient in the image taken by the IR camera of an uniform surface as seen in figure 1. To investigate how this gradient behaves when looking at uniform radiation at different temperatures we heat up a aluminium block and monitor the radiation coming from its surface. The aluminium block is first sand-blasted and then spray-painted so that it will have a homogeneous radiating surface. We drill a hole on the side of the aluminium block and put a thermistor inside it with thermal paste. The

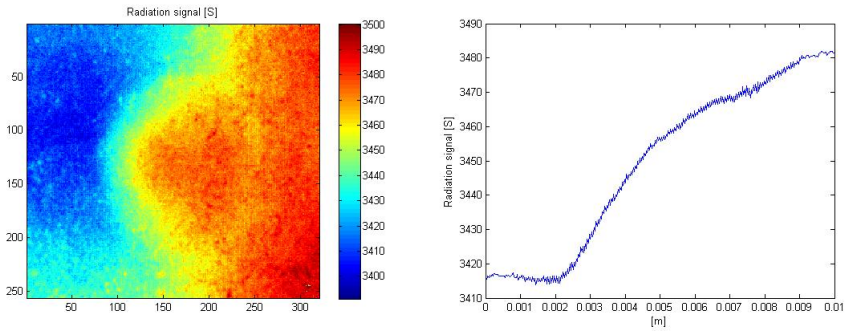

(a) Infrared image (b) Mean object signal

Figure 3.1: (a) Infrared image of the painted surface of an aluminium block at 10C°. (b) Averaging the radiation signal along the vertical direction shows an gradient in the image.

temperature of the aluminium block is controlled by a peltier element whose voltage is adjusted by the thermistor sitting inside the aluminium, see figure 3.2. The gradients we observe in the IR images for the peltier element set to

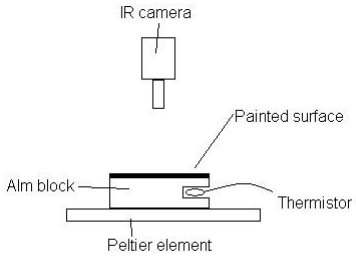

Figure 3.2: Sketch of the aluminium and the peltier element setup.

10C°, 20C°, 30C° and 40C° is shown in figure 3.1 and 3.3.

To see whether this gradient is induced by the material under vision or the infrared camera itself, we turn the peltier element and the aluminium block 180° degrees. Turning the system under view should shift the direction of the gradient too if it is caused by the aluminium and the peltier element. Contrary to this what we observe is that the the gradient remains in the same direction, meaning that the infrared cameras is causing it. Just to check whether there is a tilt that is causing the gradient we swing the camera around in both directions, but the gradient does not change direction. Considering this we subtract the image of the turned system from the initial Infrared

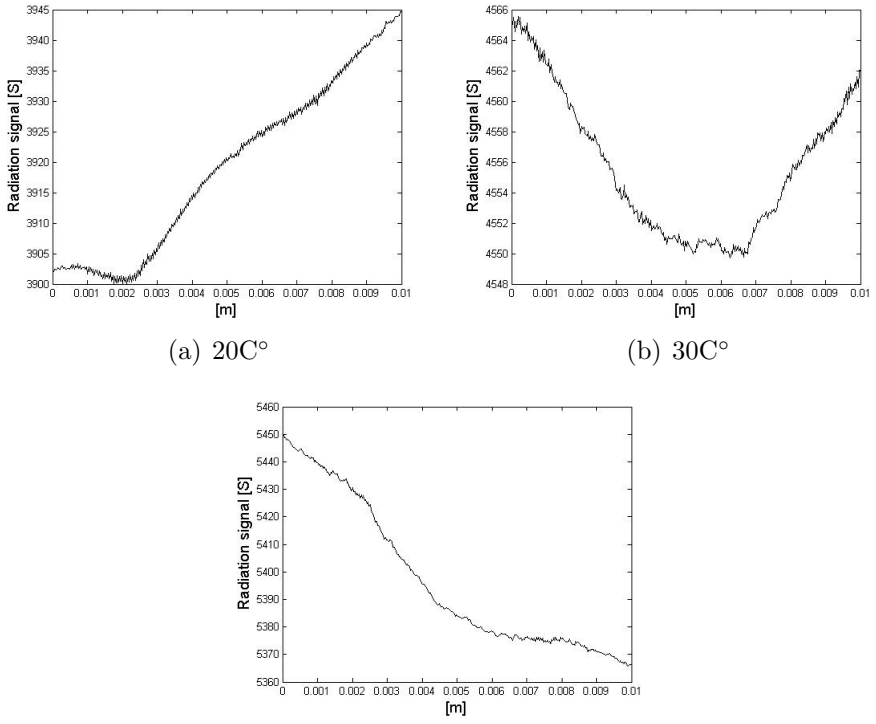

(a) 20C°

(b) 30C°

(c) 40C°

Figure 3.3: Looking at the signal gradient on the coated surface of the peltier element at different temperatures

image and plot the mean value (in the direction of the gradient) in figure 3.4 Since all the curves are very close to zero the gradient must be induced by the camera and its optics.

A special feature of this pattern is that the gradient in the image changes as the uniform radiation signal changes. Considering that the gradient is not constant it can not only be caused by the optics alone. Interesting about this feature is that when we increase the temperature of the peltier element the gradient in radiation changes to the other direction, i.e. the area that was emitting less relative to the other area, is emitting more now. At $10C^o$ we observe that the left side of the image is emitting less than the right side, and at $50C^o$ the right side emits more. When we rotate the peltier element 180^o degrees we see a slight change in the gradient but it does not change direction. This deviation from uniform radiation as we would expect must be a sum of the effects from the optics and the detector of the infrared camera. Another thing that can cause such effect is that the software used (*Ther-*

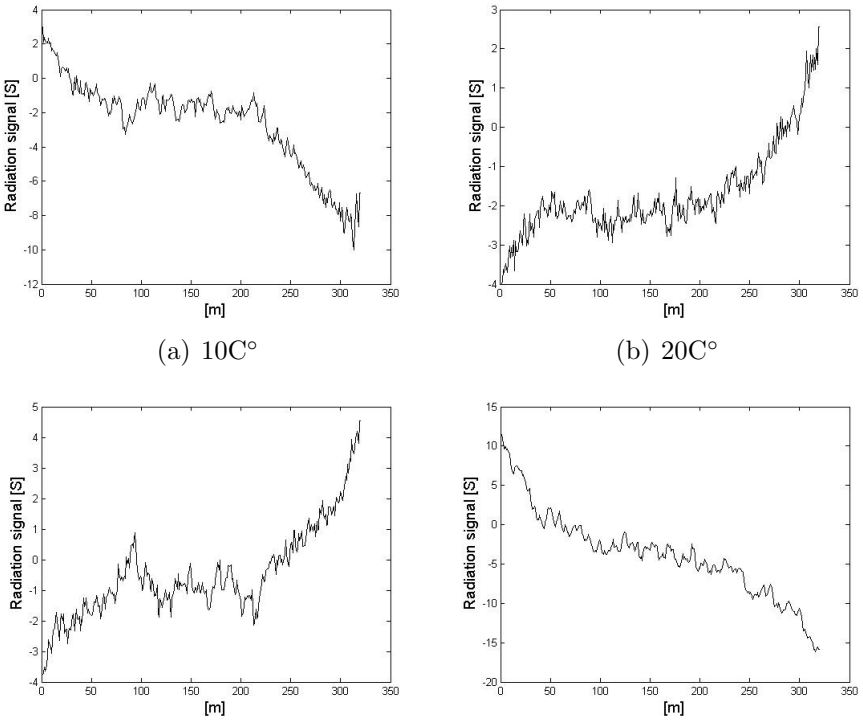

(a) 10C° (b) 20C°

(c) 30C° (d) 40C°

Figure 3.4: The mean of one image subtracted from the other. The first image is taken of the aluminium block at a certain temperature, the peltier element and the aluminium block are turned 180 degrees to check whether the gradient in the image changes direction.

macam Researcher) to interpret the radiation detected by the camera is not correcting for the detctors efficiency correctly (Non Uniformity Correction).

3.4 Increasing radiation signal at stable temperature

Another weird feature we observed was that the average radiation recorded by the camera always seemed to increase while we were looking at an uniform surface held at stable temperature. Using the peltier element we can map out this feature of the camera. we hold the peltier element surface at $22C^o$ and record an IR image and a thermistor reading every 40 sec. The result

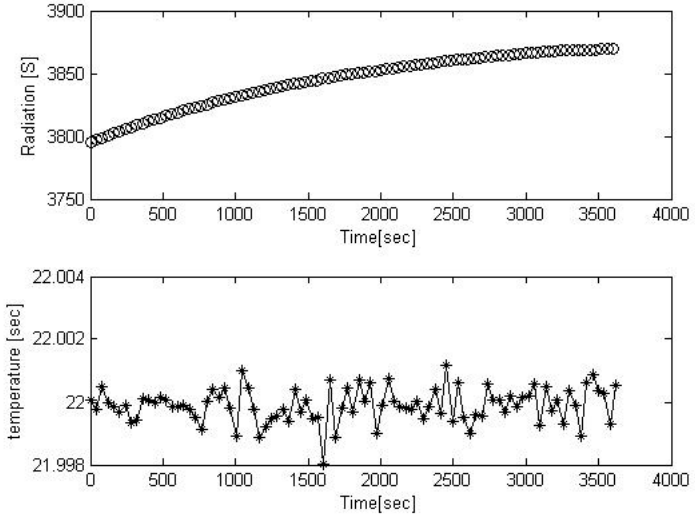

Figure 3.5: The top figure shows the radiation signal monitored by the IR camera and the bottom figure the thermistor readings recorded at the same time. While the temperature of the surface of the peltier element is held stable within 4mK as can be seen in the plot, we observe that the signal recorded by the IR camera is not stable and increases with time.

of the first recording is given in figure 2, the data recording started at 19:59, but unfortunately the recordings were started 30 minutes after turning on the camera. Still the result show the suspected behaviour that the radiation signal measured by the IR camera increases while the temperature of the peltier element is held stable. The increase in radiation signal in figure 2 is decreasing with time, which means that if we give the camera enough time, it might stabilize at a certain radiation signal. To see if it does so we do another recording for a bit longer time starting 12:48. This time we started recording at once the IR camera was ready, the data is plotted in figure 3. The reason for that the 19:59 data starts at higher point is that I started recording about 15 minutes later, after I had turned on the IR camera, compared to when I started recording the 12:48 data.

Even though the curves seems to have the same shapes the recording time they were started on is different and none of them go on for longer than 1 hour. To get a better Analysis of this feature we record for a longer time and at a different spot than previously on the peltier element. We do this twice once starting at 11:47 and second time at 12:09. The data from all four time is plotted in figure 3.7. One thing to note in figure 3.7a is that the

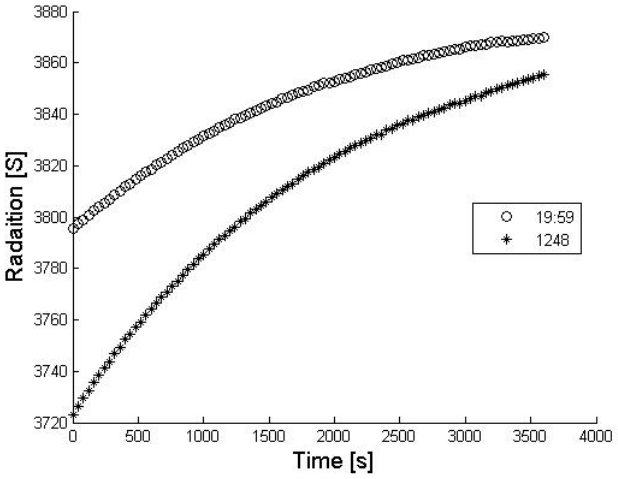

Figure 3.6: Looking at radiation increase on a surface held at stable temperature within 2mK with the PID controller.

radiation signals recorded by the camera starts at a different value for the same temperature of the peltier element in all four recordings. The first data set (19:59) starts at the highest point of all four, which can be explained by the recording started later relative to the three other datasets. One important factor contributing to that the other data sets start at different points is that the last two data sets are recorded at different spot than the previous two. Another factor is that they were recorded at different days which means that the humidity and the room temperature might be different.

To check whether this feature is induced by the camera itself and if the curves for all four recordings have the same increase pattern we arbitrarily shift the start positions so that they fall on top of each other, as shown in figure 3.7b. The curves follow the same pattern for about the first three hours, but the greater increase in radiation occurs for the first hour and a half, after this the radiation signal recorded by the camera increases very slowly. Considering that the curves collapse so well this feature of the camera must be caused by the infrared camera itself. One explanation for this might be that the detector or the optics might be warming up which increases the radiation signal measured by the camera. Knowing that there is a faster increase in radiation signal recorded for the first hour and a half, any calibration done with the camera must be done after this time. Experiments where we only record the temperature changes (radiation signal) for a short time period (e.g. $\Delta t < 10min$) will not be effected by this feature.

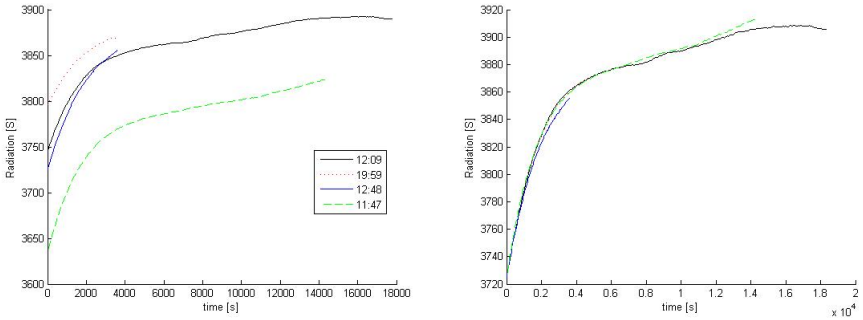

Figure 3.7: (a) Data collected of the radiation increase observed by the infrared camera for four different measurements. (b) The same data plotted on top of each other to check the similarity in the increase pattern.

Considering that the radiation signal level starts at different values for different recordings (see figure 3.7a) when looking at a surface with the same temperature ($T = 22°\text{C}$), we can not link the radiation signal directly to an absolute temperature value. We can only characterize the temperature variation during our experiment. This is because a temperature change in the material gives a characteristic radiation change which is recorded by the IR camera. How we exactly do this is explained in next section.

3.5 Calibration

Knowing these characteristics of the IR camera, we can now explore how the camera behaves when we increase the temperature. The object used to calibrate the camera is the surface of the peltier element that has been coated with anti-reflective coating. Calibration is done by increasing the temperature of the peltier element by 1^oC going from 20^oC to 30^oC. An IR image and a thermistor reading are taken for every 1 degree increase of the peltier element surface. The data collected is given in figure 3.8. To check whether the relation between the signal measured by the IR camera and the temperature can be approximated by a linear fit we compute the correlation coefficient using

$$r = \frac{1}{n-1} \sum_{i=1}^{n} \left(\frac{X_i - \bar{X}}{s_X} \right) \left(\frac{Y_i - \bar{Y}}{s_Y} \right). \tag{3.2}$$

The parameters $\bar{X}$, s_X and n are the sample mean, sample standard deviation and number of samples. The result we get for the correlation coefficient is

r = 0.9996. Considering how close this value is to 1 we can use a linear approximation with good confidence.

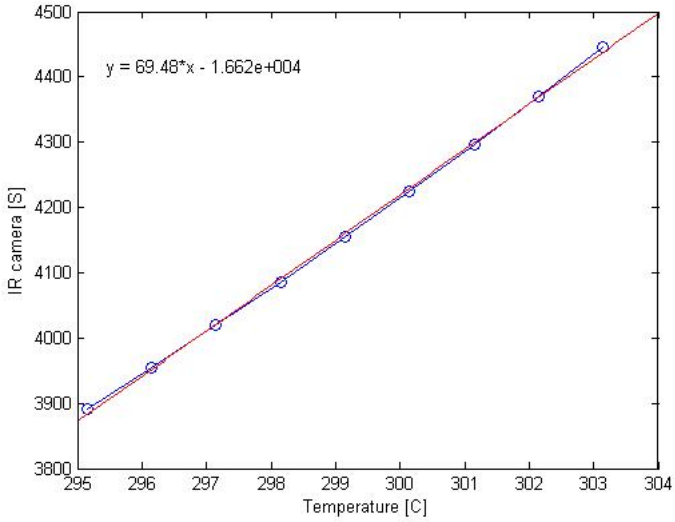

Figure 3.8: Average value of the radiation signal recorded by the camera is plotted against the temperature. Red line is the linear fitted equation and the blue dots represent the data.

The relation between the radiation signal detected by the camera and the temperature can be written as

$$IR_{cam} = \alpha T + \beta. \tag{3.3}$$

From calibrating the camera to the coated surface of the peltier element (see figure 3.8) we get $\alpha = 69.5S/K$ and $\beta = -1.66 \cdot 10^4 S$. As we have observed previously (see figure 3.7a) the constant β is not stable. We can therefore only compute temperature changes from the radiation variation:

$$\Delta T = \frac{\Delta IR_{cam}}{\alpha} \tag{3.4}$$

3.6 Comparison to the radiation from a grey body

To be able to characterize the properties of the material under study we must compare the radiation measured by the IR camera to what is theoretically emitted by a grey body in the range $\Delta\lambda$=3-5μm. The Total radiation

detected by the camera is given by the sum of the radiation emitted $\varepsilon(\lambda)$, reflected $r(\lambda)$ and transmitted $\tau(\lambda)$ by the material under view. The radiation that is reflected, $I_{bb,a}$, can be considered to be radiated by a black body at ambient temperature T_a. If the material is transparent it lets through a fraction $\tau(\lambda)$ of the radiation emitted by the surroundings $I_{bb,f}$, that can be considered as a black body at temperature T_f. Using equation 2.5 from chapter 2 the radiation detected can be written out as

$$\begin{array}{l} R_{\text{det}}(\Delta\lambda, T, \theta, \varphi) = \int_{\Delta\lambda} \varepsilon_{\Delta\lambda,\theta,\varphi}(\lambda)\, I_{bb,p}(\lambda, T_p) d\lambda + \\ \int_{\Delta\lambda} r_{\Delta\lambda,\theta,\varphi}(\lambda)\, I_{bb,a}(\lambda, T_a)\, d\lambda + \int_{\Delta\lambda} \tau_{\Delta\lambda,\theta,\varphi}(\lambda)\, I_{bb,f}(\lambda, T_f) d\lambda \end{array}, \tag{3.5}$$

where $I_{bb,p}$ is radiation emitted by a black body at the temperature of the peltier element surface T_p.

The use of the black anti-reflective coating allows us to neglect the last two factors of equation 3.5 which correspond to the radiation reflected and transmitted through the material. Moreover we only interpret changes in radiation and temperature of the material, while the change in the room temperature and surroundings can also be neglected. If we change the temperature of the peltier element from $T_p = T_1$ to $T_p = T_2$ the equivalent radiation change measured is (constant emissivity)

$$\Delta R = \varepsilon_{\Delta\lambda,\theta,\varphi} \int_{\Delta\lambda} \left[I_{bb}(T_2) - I_{bb}(T_1) \right] d\lambda. \tag{3.6}$$

Before comparing this equation with the radiation measured by the IR camera we have to integrate it, and since this integral can not be integrated analytically we must use a numerical integration technique. For this we develop a numerical integration code made in matlab, it is given in appendix 3. This code integrates Planck's law for a given temperature and waveband. We checked the accuracy of this code by comparing its results to the ones from an integration table in the book *Infrared Thermography*[9]. To be completely sure about the codes performance we check if the integration result converges towards a function that is directly proportional to the 4th power of the Temperature as it should be according to Stefan Boltzmanns law

$$R = \frac{2\pi^5 \kappa^4}{15 c^2 h^3} T^4 = \sigma T^4. \tag{3.7}$$

Testing this we discovered that the convergence does not apply before most of the waveband is covered.

Integrating Plancks law for $\Delta\lambda$=3-5μm numerically, we plot it against the result we get from the IR camera at the same temperatures of the peltier element surface recorded by the thermistor, see figure 3.9. From this plot we

see that there is a linear relationship between the radiation signal measured and the theoretical radiation emitted by a blackbody (correlation coefficient r=1.000). This relation tells us that our assumptions that we can neglect the radiation changes because of reflection and transmission and that the emissivity is constant for small temperature changes are consistent with the measurements.

From this linear relation we can relate the object signal and the unit $[S]$ that the infrared camera gives out to the radiation emitted by a black body. Taking the coated peltier element surface as an example, which is a grey body and emits a fraction ε of that emitted by a black body $I_{blackbody}$. Of the total radiation that is emitted from the surface of the peltier element a fraction $\varepsilon_{\Delta\lambda,\theta,\varphi,T}$ is captured by the camera, and this radiation is enhanced by a factor A_{cam} before given out as a measurement in the unit $[S]$. The linear relation can the be written as

$$IR_{cam} = A_{cam}\varepsilon_{\Delta\lambda,\theta,\varphi,T} I_{blackbody} + B_{cam} = A_t I_{blackbody} + B_{cam}. \tag{3.8}$$

The only factor that can change in the gradient $A_t = A_{cam}\varepsilon_{\Delta\lambda,\theta,\varphi,T}$ is the emissivity, therefore for a material that has a constant emissivity should always have the same gradient A_t. The other constant B_{cam} changes with the conditions of the surroundings (the room temperature, humidity, amount of radiation reflected and transmitted), as seen already in figure 3.7a. Conducting a linear fit between the data plotted in figure 3.9 gives $A_t \approx 1051\frac{S}{J/s\cdot m^2}$ and $B_{cam} \approx 2251S$. To investigate this relation further and better we recorded the radiation signal for temperatures from 10^oC to $50{,}5^o$C with 0.5 degree jumps, the data is plotted in figure 3.10. The gradient between the radiation signal and the theoretical radiation emitted by a black body for this data is $A_t = 1028\frac{S}{J/s\cdot m^2}$ (see equation 3.8), which is close to the previous estimation.

The relation between the temperature and the radiation signal is non-linear for large differences in temperature (see figure 3.10a), but when we look at small temperature differences the relation is linear (see figure 3.8). Therefore any calibration that relates the temperature changes directly to the radiation signal change recorded by the camera should be done for small temperature differences ($\Delta T < 10C^\circ$). we will therefore in all calibrations plot the absolute temperature measured by the thermistor against the radiation signal recorded by the camera, so that it is clear in what temperature range the camera is being calibrated. Even though when we relate the radiation signal with temperature we only make use of the gradient given by the linear fit from these two datasets, only interpreting temperature changes and not absolute values.

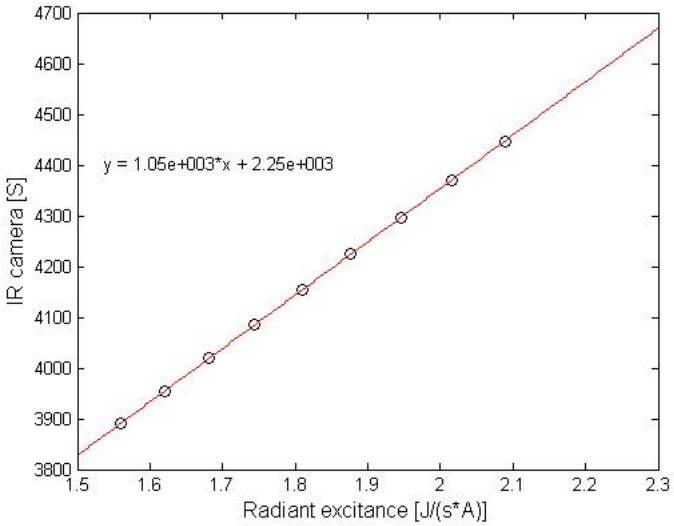

Figure 3.9: The radiation signal recorded by the infrared camera plotted against the theoretical radiation emitted by a black body for the same temperature and waveband.

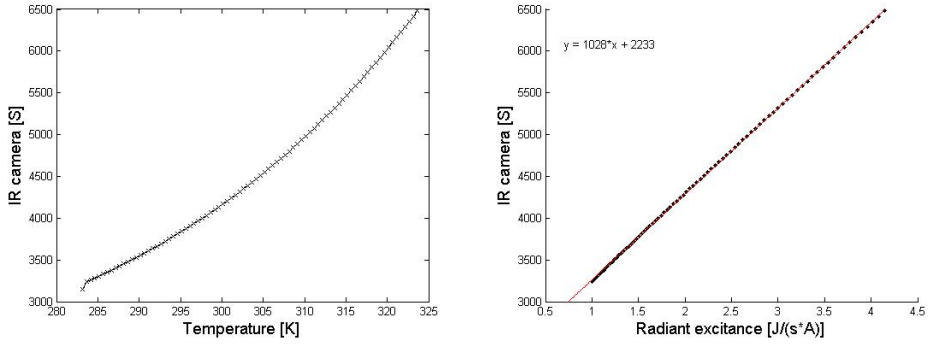

(a) IR vs temperature

(b) IR vs theoretical radiation

Figure 3.10: (a) The radiation signal monitored by the camera plotted against the thermistor measurements for a total change of $40C^{\circ}$ in temperature. We observe a non-linear relation between the temperature and the radiation signal. (b) The radiation plotted against the theoretical radiation emitted by a black body.

Chapter 4

Sandpaper experiments

The frictional sliding experiments we developed are a continuation of the work of Karen Mair and Francois Renard published in GRL 2006 [20]. The objective is to obtain an estimate of the heat dissipation during friction/fracture processes. We will use an IR camera to observe and follow the wear process. The first step will be to calibrate the camera. Then we will have to analyze carefully the radiation signal recorded by the IR camera. In particular the emissivity changes due to variation of the topography on the surfaae of the crystal during the friction experiments (plastic deformation, roughening, fractures), were not taken into account in previous work [20]. Therefore we will check here if we can neglect such effects to obtain a reliable estimate of the heat dissipated during the abrasive processes occurring during the friction experiments.

4.1 Experimental setup

The experimental setup is the same used by K. Mair and F. Renard in GRL 2006 [20], and it is shown in figure 4.1. The halite (NaCl) crystal is held under a normal load, marked as dead weight in the image. This dead weight consists of lead blocks of various mass (given in table 4.1) being placed evenly on top of an aluminium block (1.705kg) where the halite crystal is glued to. Under the crystal is a coarse sandpaper (Struer #80 grit)and the dimensions of the average halite crystal are approximately $3\times3\times0.7$ cm^3. The sandpaper is dragged at a constant velocity by pulling the bottom plate, using a stepping motor. During this sliding the sandgrains on the sandpaper dig into the surface of the crystal and create the characteristic gouge. Horizontal and vertical displacements are monitored using linear variable displacement transducers (LVDT) with sub micron resolution. We also measure the shear

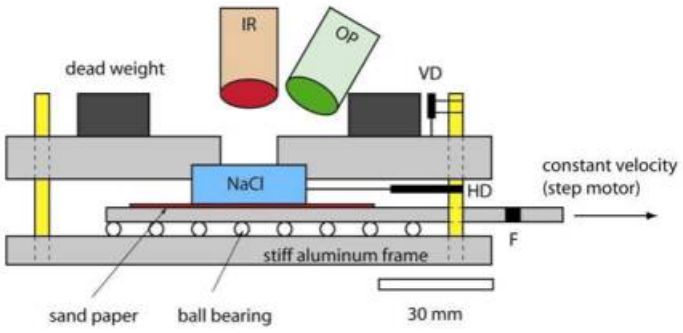

Figure 4.1: Sketch of the experimental setup, taken from [20]

Table 4.1: Weight of the led blocks

	1	2	3	4	5	6	7
led block [g]	2×415.6	882.6	2×850.2	2×1726	1697	3484.1	815.5

force imposed on the sliding block by the motor using a load cell. All these parameters are recorded at 2kHz.

Since halite is highly transmissive in the region 3-5μm, we can monitor the infrared radiation emitted at the sliding surface using a high resolution infrared camera and estimate the heat dissipation from it. The infrared camera is located above the halite sample, as indicated in figure 4.1, and focused at the slider interface undergoing shear. We used a Indigo Phoenix-mid infrared camera with InSb detector with a cold filter bandpass for 3-5μm. The result is a time-lapse movie of the radiation emitted during frictional sliding, with 256×320 pixel images captured at a rate of 50 frames per second(fps). With the optics we use in the experiments the field of view is 8×10mm.

4.1.1 Experiment OS058

When the sandpaper starts moving the asperities/sandgrains dig into the salt crystal. The crystal moves downwards as the sandgrains dig deeper into the surface, until the scratching process reaches a steady state. The sandgrains plastically deform the surface leaving scratch lines behind them, and push the material in front to the sides of the groove. Dragging the sandpaper 1.7mm/s with total normal load of 6.80 kg gives the mechanical data result

plotted in figure 4.2. From the data shown in figure 4.2 we see that the noise

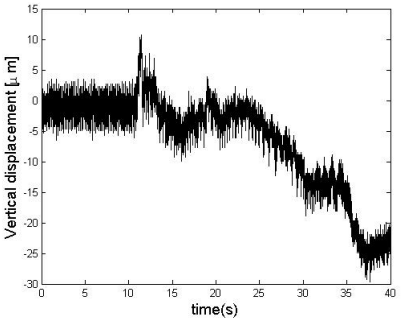

(a) Vertical displacement

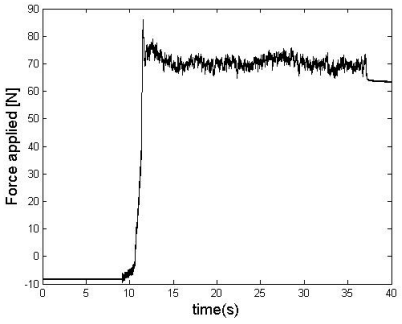

(b) Force

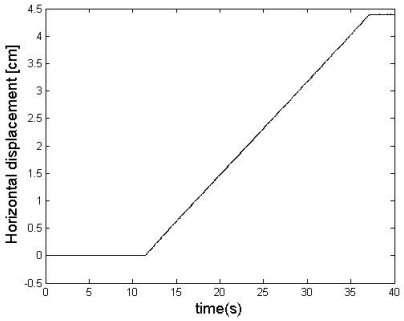

(c) Horizontal displacement

Figure 4.2: The mechanical data collected in experiment OS058. (a) The vertical displacement plot shows that the crystal moves down as the sandpaper is dragged and after it stops it slowly starts moving back upp again. The force measum. (b) The force increses as the dragging begins and holds itself stable between 64-78N.

in the horizontal displacement plot is much lower relative to the total change in position. In the case of the vertical displacement we have much more noise relative to the total displacement at the end. The sandpaper is dragged for approximately 25 seconds a total distance u_{hor}= 4.4cm and during this the maximum vertical displacement the crystal moves is u_{ver}=25.36μm. At the same time we observe and follow the abrasive process at the interface between the bottom surface of the crystal and the sandpaper, with an infrared camera. A typical image recorded by the camera during an experiment is shown in figure 5.8. The aim will be to obtain a quantitative estimate of the heat dissipation during the sliding, and to evaluate the temperature increase at the surface of the crystal.

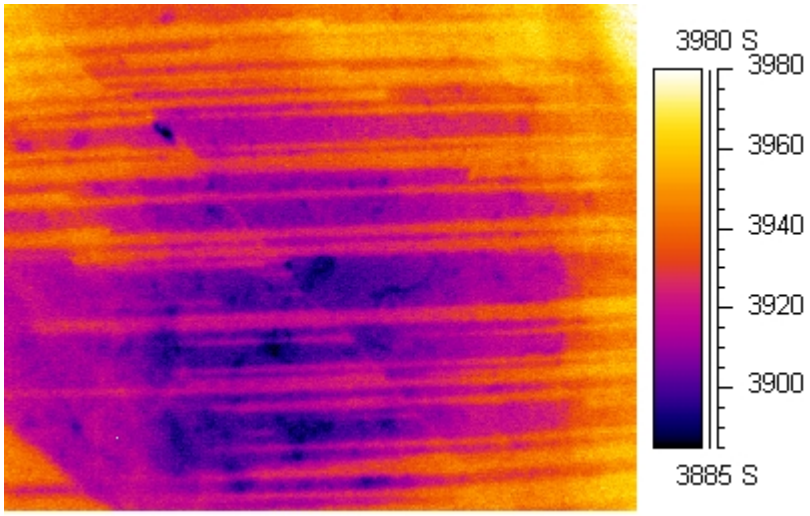

Figure 4.3: Infrared image of the sandpaper being dragged across the surface of the crystal with the dimensions 8×10mm. The colorbar shows the radiation recorded by the infrared camera. We can link the variation of the amplitude of this signal ΔS to variation of temperature ΔT see chapter 3.4. The bright lines are scratches being made on the sliding surface of the crystal.

4.2 Calibration

The method of calibration we used on this system is the same as in chapter 3.4, but instead of a Peltier element we will use a Hot plate. We place the sandpaper on the hot plate and the halite crystal on top of it. To read temperature and radiation changes at the same time we make a scratch in the crystal large enough to fit a thermistor bead. Graphic description of this setup is given in figure 4.4. The infrared camera has a top view of this setup with the sandpaper and crystal interface in focus, the thermistor is also inside the optical field of the camera, see figure 4.4b. To block out the radiation changes because of reflection of objects such as lights, people etc. We enclose the sandpaper in polystyrene box and only have a hole on top of the box, which the infrared cameras lens pokes through. Walls inside of the box are made of cardboard so that there is a uniform surface radiating into the object. When We spin the box around the sandpaper and the crystal we do not observe any change in the radiation signal recorded by the camera.

Each time we turn up the temperature of the hot plate we wait (up to 15min) till the thermistor reading is stable within $\Delta T = \pm 0.07K$. Then we note the average radiation in the area marked in figure 4.4b and the thermis-

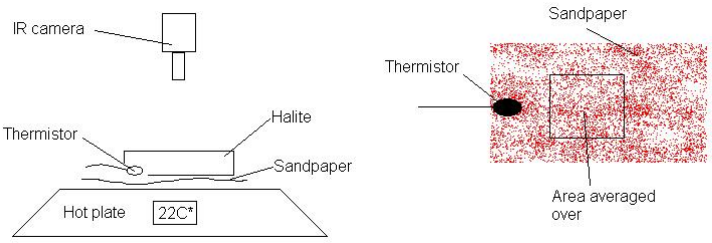

(a) sideview hot plate (b) IR view of hot plate

Figure 4.4: (a) Sketch of the calibration setup. The thermistor is used to calibrate the radiation change monitored with the infrared camera to the temperature difference measured at the interface between the crystal and sandpaper.(b) Sketch of the calibration setup seen from above. The radiation monitored in the square area is used for calibrating the infrared camera.

tors resistance value. Plotting the radiation signal against the temperature gives a linear relation with a gradient of $\alpha = 86$, see figure 4.5. As explained in chapter 3.4 we can only interpret radiation signal change into temperature change using the gradient α and the equation 3.4, and not an absolute value using the linear relation.

We plot the radiation signal measured by the infrared camera against radiant excitance of a blackbody

$$\Delta R_{bb}\left(\Delta\lambda, T\right) = \int_{\Delta\lambda} I_{bb} = \int_{\Delta\lambda} \frac{2\pi hc^2\lambda^{-5}}{e^{\frac{hc}{\lambda kT}} - 1}$$

between $\Delta\lambda = 3 - 5\mu$m, where h, c, k and T, are the Planck's constant, the Boltzmann's constant, the speed of light and the temperature respectively. The plot shows a linear relation between the radiant excitance ΔR_{bb} and the radiation signal IR_{cam}, as it should according to the equations 3.6 and 3.8, with a gradient of $A_{cam} = 3.4e2$.

Before applying this result to the experiment, we have to be aware of various sources of possible errors and differences between the setup used here and the one used during the sliding experiment. One major difference in the calibration setup and the experimental setup is that the hot plate under the sandpaper also gets warmer when heating the sandpaper and crystal, and some of its radiation change transmits through to the infrared camera. In contrast to the experimental case where heating happens beacuse of plastic deformation or friction, the sandgrain and the crystal are the only parts that get warmer. If the temperature of the sandgrain changes from T_1 to $T_2$the

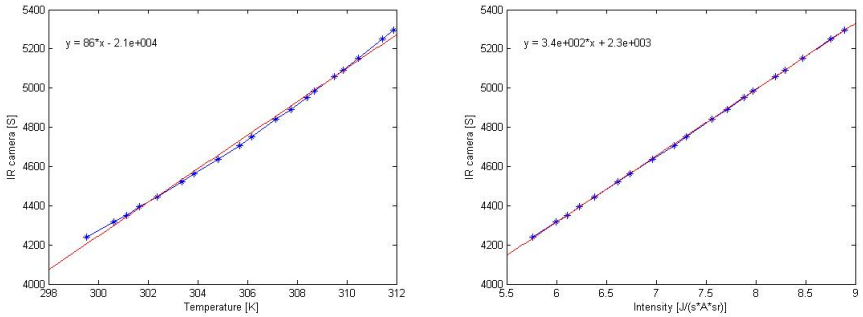

(a) IR camera vs Temperature (b) IR cam vs radiant excitance

Figure 4.5: (a)The radiation signal recorded by the infrared camera plotted against the temperature measured by the thermistor. The plot shows a linear relationship between the Radiation signal and the temperature. (b) Plotting the radiation change monitored by the infrared camera against the theoretical radiation change of a blackbody between $3-5\mu$m for the same temperature. The slope in this relation is dependent on the emissivity and should remain constant in chapter 3.5

equivalent radiation change measured by the camera would be

$$\Delta R_{exp} = \varepsilon_{\Delta\lambda,\theta,\varphi} \int_{\Delta\lambda} \left[I_{bb}\left(T_2\right) - I_{bb}\left(T_1\right) \right] d\lambda, \tag{4.1}$$

where $\varepsilon_{\Delta\lambda,\theta,\varphi}$ is the directional emissivity of the system under view and I_{bb} is the radiation emitted by a blackbody at temperature T. In the calibration setup we monitor the radiation change

$$\begin{aligned} \Delta R_{calib} &= \varepsilon_{\Delta\lambda,\theta,\varphi} \textstyle\int_{\Delta\lambda} \left[I_{bb}\left(T_2\right) - I_{bb}\left(T_1\right) \right] d\lambda \\ &+\tau_{\Delta\lambda,\theta,\varphi} \textstyle\int\limits_{\Delta\lambda} \left[I_{hot\_plate}\left(\lambda, T_{hp,2}\right) - I_{hot\_plate}\left(\lambda, T_{hp,1}\right) \right] d\lambda \ . \end{aligned} \tag{4.2}$$

where the first part is the same as the radiatoin change of the sandgrain in the experiment and the second part is the radiation change of the background multiplied by the tranmissivity $\tau_{\Delta\lambda,\theta,\varphi}$ of the sandgrain and the crystal. The calibrations have an additional radiation change compared to the experiment whose effect is determined by the transmissivity $\tau_{\Delta\lambda,\theta,\varphi}$. Other sources of error that must be mentioned are; there might be a difference in the emissivity between having a tight contact between the sandpaper and the crystal (experiments), and just having a halite crystal placed on top of the sandpaper (calibrations). Another error source is that when we enclose the sandpaper and the crystal inside the polystyrene box and turn up the hot plate, we

inevitably increase the temperature and the relative humidity of the whole enclosed system.

Let us now analyze the radiation signal during a sliding experiment.

4.3 Radiation signal analysis

Our aim with this analysis is to know how much energy is dissipated in heat during the abrasive process. For that we will have to look at the scratched area in order to determine what is the part of the radiation signal change detected by the camera inside the groove caused by heating.

If we look at experiment OS058, discussed earlier in this chapter, we are simultaneously creating many scratches at the crystal surface, see figure 4.6. The surface of the crystal inside the grooves is plastically deformed. The change of the topography of the surface contributes to the radiation signal change recorded by the camera. After the sliding experiment, we can see in figure 4.6c that the grooves created emit more radiation (bright lines) than the undeformed surface. Monitoring the radiation changes in one small area where we know the crystal is going to be scratched gives the profile plotted in figure 4.6d. We only plot the radiation signal behaviour of one scratch, but we see similar pattern in all the scratches that are created in the crystal. As one can see there is a fast increase in radiation as the sandgrain comes inside the monitored area and then there is a peak at 3923 S.

Thereafter the radiation signal slowly decreases and reaches a stable value corresponding to 3916 S, which is higher than its initial value. Since the radiation does not decrease to the initial radiation level the increase of radiation level too 3916 S is due to change of emissivity caused by modification of the topography with the creation of the groove. For the same reason, the amount of radiation that does decrease is too difficult to interpret as a heat signal.

We also tried to monitor the radiation signal with a different infrared camera, borrowed from professor Knut Jørgen Måløy from the complex group at the physics department at the university of Oslo. The camera is a ThermaCAM SC3000, and has a gallium arsenide (GaAs) quantum detector sensitive in the range 8-9μm. We carry out experiment OS062 with the velocity 1,7mm/s and the maximum normal load we can apply 14.6kg. We expect in this condition to have a bigger increase of heat dissipated during the abrasive process.

In order to avoid the problem of the variation of emissivity due to topography change, we analyze signal radiation at the groove tip when we stop dragging the sandpaper. The results are plotted in figure 4.7a. First there is a sharp radiation increase as observed in experiment OS058, but when we

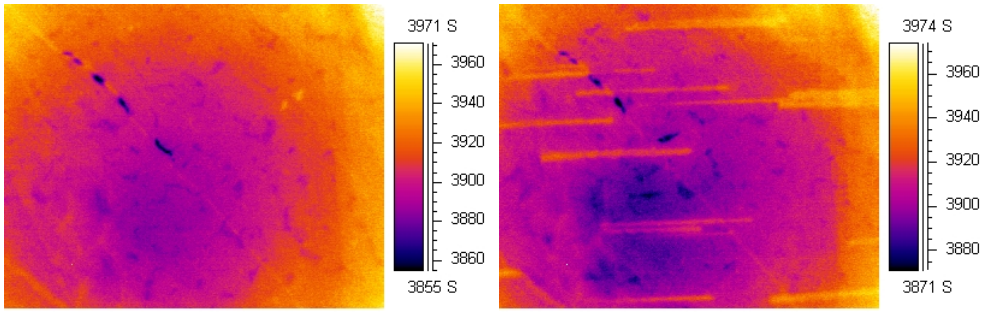

(a) IR start image

(b) IR image during scratching

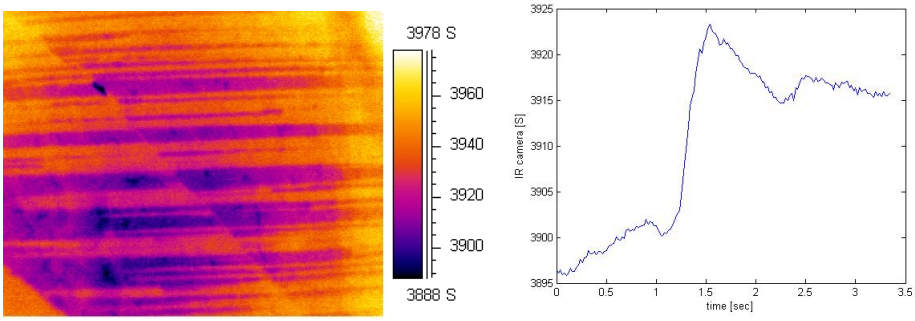

(c) IR image at the end

(d) Plot of the radiation suddenly collapsing

Figure 4.6: (a) Infrared image of the sandpaper seen through the halite crystal. (b,c) Image of the sandpaper during sliding. The bright lines are scratches on the sliding surface of the crystal. (d) The radiation signal viewed at a specific location where a sandgrain scratching the crystal passes. The amount of radiation that does not drop again happens because of emissivity changes.

stop dragging the sandpaper the radiation drops down almost immediatly to its initial level.

We convert this radiation signal to temperature using the calibration done previously in the chapter. The result is plotted in figure 4.7b. We observe an increase of temperature of $\Delta T = 0.37K$ and then a rapid decay towards the same initial value. Therefore we might be able to relate this jump in the radiation signal recorded by the camera as a flash of temperature due to a sandgrain scratching the surface of the crystal. Since we are monitoring the radiation signal at the sandgrain which is eroding the crystal, we can assume that this increase of temperature is local at the groove tip within the sandgrain (point source hypothesis). Moreover, we can consider that the

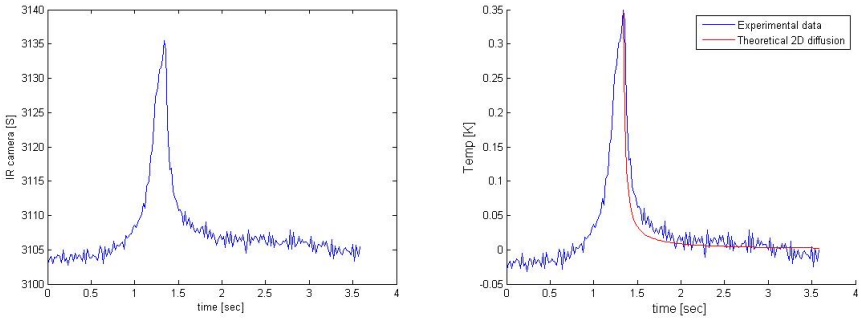

(a) Radiation signal (b) diffusion comparison

Figure 4.7: (a) Radiation signal averaged over a small area where the sandgrain stops. The radiation increases as the sandgrain approaches the field of view and then there is a steep increase as the sandgrain comes inside the small area averaged over. When the sandpaper is stopped the radiation drops quickly down. (b) The radiation signal converted into temperature.

diffusion process is in a two dimensional space within the sandgrain, which has a thermal diffusivity of $k = 9.7 \cdot 10^{-7} m^2/s$. With those two assumptions we can obtain how the temperature signal at the groove tip will decay in time:

$$T(x, y, t) = \frac{A'}{2\pi kt} e^{-\left(x^2+y^2\right)/4kt}, \tag{4.3}$$

where k is the diffusion constant, $x - y$ are the spatial variables, t is the time. More details concerning the analysis of the diffusion process will be given in chapter 6. The parameter A' (in Km^2) is chosen in order to consider the same increase of temperature given by the infrared camera. Since the radiation signal is averaged over a square around the sand grain we integrate equation 4.3 over an equivalent area. We can now compare how this local increase of temperature decays in time with the experimental signal measured by the camera. We observe in figure 4.7b that the relaxation of the radiation signal recorded by the camera converted into temperature is very close to the decay predicted by a point source diffusing in 2D (equation 4.3). This tells us that this radiation signal might actually be caused by heating on the sandgrain.

However, we know that there is a permanent change in the topography of the surface of the crystal caused by the sandgrains scratching the sliding surface that leads to a radiation increase at the tip of an groove (that does not decay), see figure 4.6d. When dragging the sandpaper we observe that the crystal has a vertical displacement and in particular when we stop the sliding the crystal moves slowly upwards again relatively to the sandpaper,

resulting in that we no longer have a tight contact between the sandgrain and the crystal. This is shown in figure 4.8, we see that as the sliding stops (time$\approx$ 37) the crystal starts moving upwards. This variation in the vertical

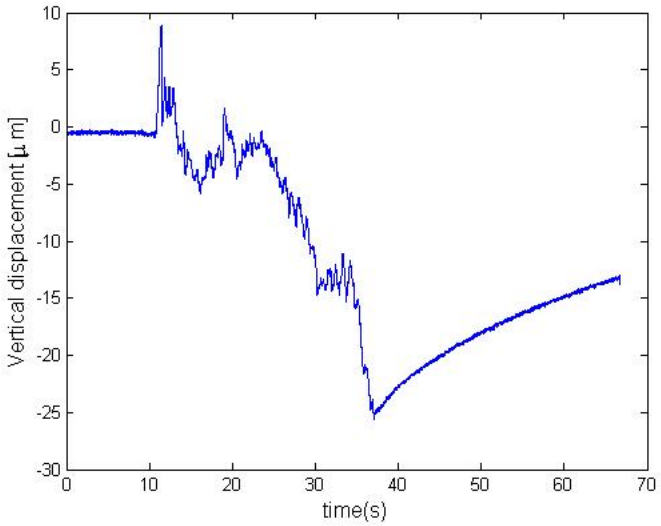

Figure 4.8: Radiation signal averaged over a small area wh

displacement could change the radiation signal measurement.

Therefore it is impossible to conclude that the change of the radiation signal given by the camera is only caused by heating at the sandgrain eroding the crystal. It is impossible to distinguish in this signal which part is due to a change in emissivity, caused by surface topography change or vertical movement of the crystal, and which part is related to a local variation of temperature. The radiation signal a bit away from where any surface deformation is happening is too small ($\Delta IR_{cam} < 3S$) and in the noise of the camera to quantify as heating. Therefore it is impossible to interpret the variation of the radiation signal as heat dissipation in the sliding experiment.

4.3.1 Painted crystal

The reasons for why we are having difficulties estimating the thermal heating in the sandpaper is that there are to many processes happening at the same time and because the sandpaper is a non-homogenous radiator. To fix this problem we paint the sliding surface of the crystal with black anti-reflective coating, so that almost no radition from the sandpaper transmits through the paint. Running experiment OS066 with a painted crystal with same

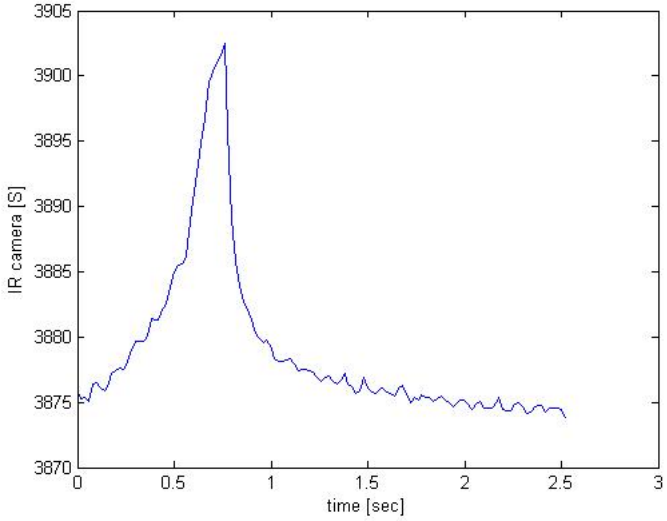

Figure 4.9: Radiation signal monitored at the tip of the scratch with ThermaCAM SC300 in experiment OS066. We observe the same pattern as with the sandpaper experiments.

velocity and weight as in experiment OS062 gives the result, monitored with ThermaCAM SC300, shown in figure 4.9a. We again stopped dragging the sandpaper early to monitor the radiation profile at the tip of a scratch. The radiation profile does not change with painted surface and neither is there a radiation increase and deacrease large enough on the sides of the groove to identify as heat (remains in the noise). We observe the same behavious in the radiation signal as for previous experiments.

4.4 Point heating in the halite crystal

From the experiments analyzed so far the only thing we can conclude is that we can not distinguish the radiation signal caused by heat from that caused by emissivity changes. To investigate how the radiation signal recorded by the camera on the painted bottom surface of the crystal would behave if we artificially heated up halite crystal we heat small spot of the crystal. We do this by placing a small nail on top of the peltier element and the crystal on top of it again such that the nails tip barely touches the crystal, see figure 4.10a. We place a square paper with a black paint layer around the nail in order to block radiation changes from the peltier element. Heating the peltier element

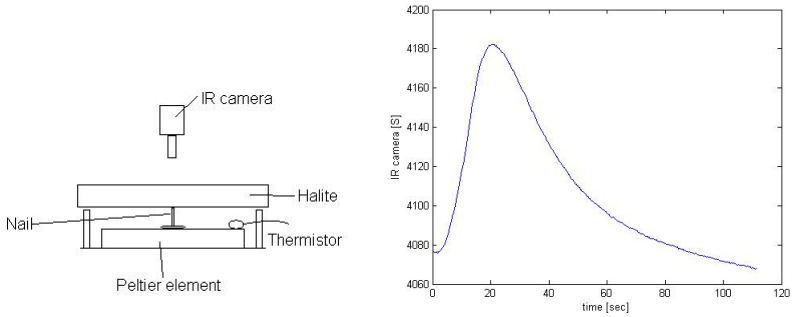

(a) Sketch of the setup (b) Radiation signal

Figure 4.10: (a) The painted surface of the crystal is heated by the nail placed under it. (b) The radiation increases as the temperature of the nail increases and when the peltier element under the nail is turned off we have a slow thermal diffusion.

about 10C° and then suddenly turning it off gives the radiation signal plotted in figure 4.10b. The radiation increases about $\Delta IR_{cam} = 100$S, equivalent of temperature change of $\Delta T = 1.4$K according to the calibration in chapter 3.5, and then after turning off the peltier element the radiation slowly decreases. One problem with this setup is that the nail remains in contact with the crystal the whole time, resulting from this the radiation change we monitor may come from the nail and not the paint. Since it is the crystals properties we want to analyze we will have to remove the nail after heating up the crystal. For this purpose we place the peltier element on a plate that can be suddenly pulled downwards thereby removing the nail from the IR image, and the crystal is held still by a extension clamp. The result of this is given in figure 4.11. As in the experiments we see a sharp drop in the radiation when the nail is removed, meaning that most of the signal is coming from the nail not the crystal or the paint. Considering that from none of these two setups were we able to look at the heat signal solely from the crystal, we must find a method that heats up the crystal without touching it.

4.4.1 Heating the crystal white light

In order to heat the crystal without touching it we focus the light from a lamp on the painted surface, so it can absorb maximum energy from the light beam (see figure 4.12). The halite crystal is held by a extension clamp and we place a thermistor covered in thermal paste on the painted surface. To focus the light from the lamp into a small point on the crystal we use

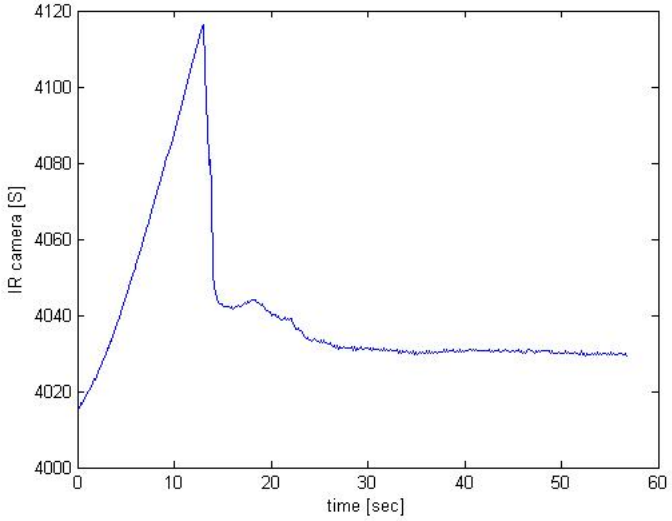

Figure 4.11: Radiation signal from removing the nail after heating. The amount radiation that drops sharply when the nail is removed comes from the nail and not the heating of the painted surface.

a magnifyer, whose beam converges into a circle of about 1cm in diameter. The thermistor is about 1.5cm from where the beam converges. The radiation monitored by the infrared camera and the heat by the thermistor are plotted in figure 4.13. The increase in radiation measured by the camera and the increase detected by the thermistor have a very similar rising shape. When the lamp is turned off the radiation has a initial quick drop of about 130S that can be related to the reflection of the light. Then the two different signals decrease in the same way. Since there is no other process happening after the lamp is turned off on the surface of the crystal we can conclude that it is actual temperature that is diffusing inside the crystal to the surroundings.

4.5 Conclusion

During all the various sliding experiments performed using sandpaper the radiation signal measured by the infrared camera can be modified a lot by a change of emissivity due to variation of the topography of the surface of the crystal (with the creation of the groove, with brittle and plastic deformation and the contact point of the sandgrain eroding the crystal). Since it is to difficult to interpret this radiation signal, it is impossible to affirm that we

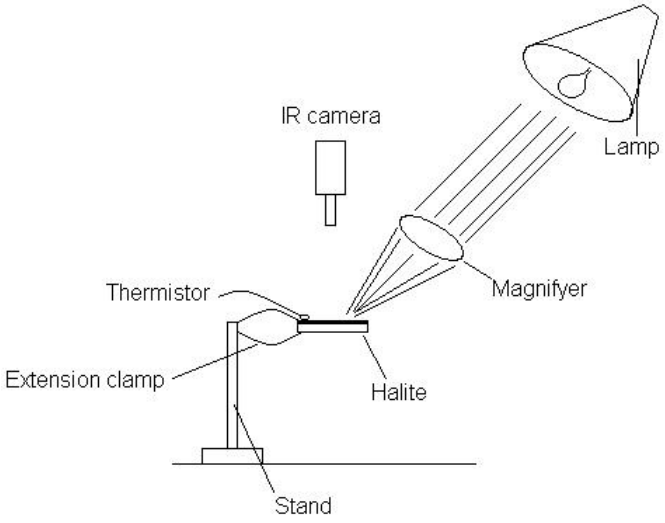

Figure 4.12: Sketch of heating the crystal with a lamp and magnifyer without any physical contact

observe heat production and dissipation during those frictional sliding experiments, and confirm the results shown in the paper *Thermal imaging on simulated faults during frictional sliding* [20].

However we will propose in the next chapter a simpler setup and configuration that will allow us to observe and investigate quantitatively an increase of temperature and heat dissipation at the surface of the crystal during friction processes.

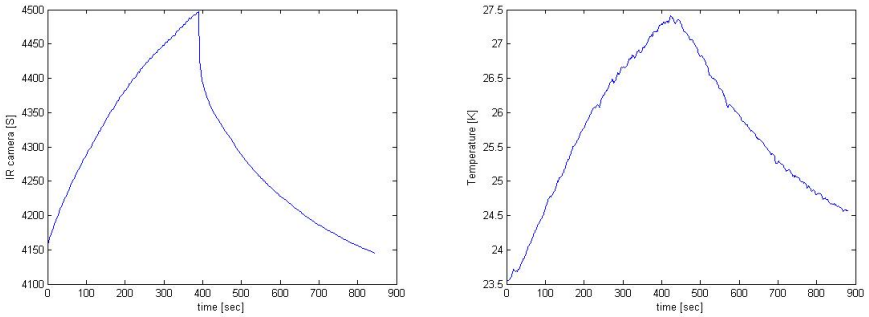

(a) Radiation signal (b) Thermistor reading

Figure 4.13: Plots of the radiation monitored on the surface of the painted crystal and the temperature measured with a thermistor. We measure actual temperature diffusion of the crystal surface with the infrared camera.

Chapter 5

Single indenter experiments

When we drag the sandpaper across the surface of the crystal there are many scratches that are being created simultaneously. The vertical displacement data we get out from these experiment have the contribution from all of these processes, the same goes for the shear stress measured by the load cell. The heterogenities on the sandpaper have different size and therefore it creates fractures and grooves with different sizes and depths. Therefore the force and the heat dissipated during those sliding experiments will vary locally along the surface of the crystal. In order to quantify and characterize the heat dissipated during a frictional sliding experiment, we need to simplify the experimental setup previously studied. Instead of using a sandpaper with several sand grains scratching the crystal we will use now a single indenter eroding the crystal.

5.1 Various type of indenters

The single indenter has to be similarly shaped as the sand grains on the sandpaper. It must also be elevated enough above the aluminium so that the crystal only touches it, translating all the forces into making the groove. To have an indenter with those features we take a screw and grind the tip into a needle shape as shown in the sketch below (figure 5.1). The tip of the screw is flat with the dimensions; 1mm in diameter and 1 cm long. The indenter is screwed to the bottom plate (aluminium board), so that only the tip sticks out from the aluminium. One interesting feature of this setup is that we can adjust the angle of the indenter by making a tilted hole in the aluminium plate. We can also shape the tip of the screw as a cone or a half sphere to see the effect of the shape on the mechanics of the indentation.

With the indenter screwed to the bottom plate and the crystal attached

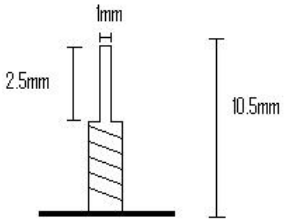

Figure 5.1: Sketch showing the dimensions of the screw indenter. The salt crystal is held still on top of this indenter with only its tip in contact with the crystal. The screw is then dragged with the bottom aluminium plate that it is attached to, making a scratch on the crystal surface.

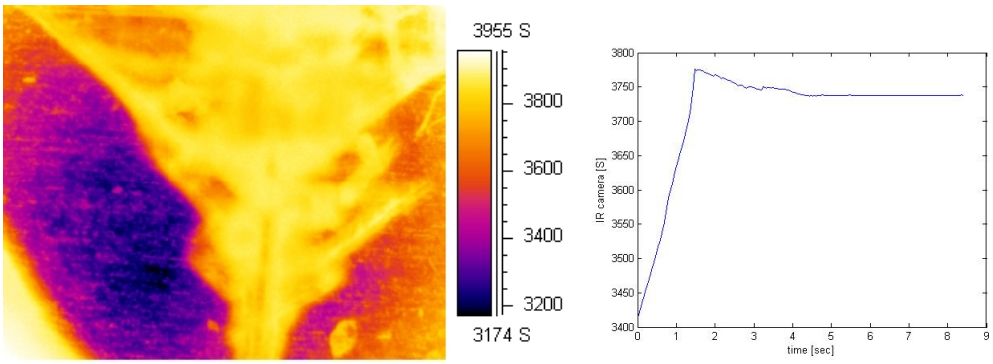

(a) The crystal deformed

(b) IR signal

Figure 5.2: (a) Infrared image of halite crystal after it has been deformed by an screw indenter. (b) Radiation signal observed at a small area where the tip of the indenter passes.

to the top as before we are ready do an indentation experiment. We must be very careful on how much normal force we apply since the crystal might break under to much pressure. Therefore we use no deadweight since all the normal force will be applied to the single groove and not distributed over several as in the case of a sandpaper. The only normal force applied will be from the plate the crystal is attached to which has a mass of 1.705kg, this translates into a pressure of $sigma = 21MPa$ at the tip of the indenter. We ran experiment OS059 with this setup. We had to stop the experiment, since the screw went too deep into the crystal, and started to break big chunks of

it. An infrared image of the damaged surface is given in figure 5.2a. Since the minimum normal force we can apply with this setup is to great for the halite crystal, we need to change the type of indenter.

5.2 Glass bead

Now we use a glass bead that has a smooth spherical surface, distributing the normal force over a larger area (the average diameter is 1mm). The glass bead needs to be attached to the bottom aluminium plate. To do this we make a small dent in the aluminium by pushing down a tool with sharp tip. Then we glue the glass bead into this dent. A sketch of a glass bead attached to the bottom plate is given in figure 5.3. We run experiment OS082 with

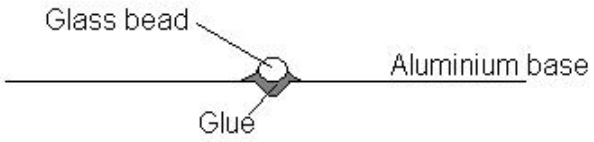

Figure 5.3: Sketch of a glass bead attached to the bottom aluminium plate. The crystal is held still on top of this glass bead, and then the bead is dragged to make a scratch.

this setup at the velocity 1.7mm/s and normal load 3.4kg, which translates into a pressure at the glass bead contact of abpot $\sigma = 42MPa$. From looking at the crystals indentation surface afterwards we see that the indenter did not cleave through the crystal as it did in the screw indenter case.

5.2.1 Mechanical processes

From this experiment we get a quantitative measurement of the force and the vertical displacement caused by single indenter scratching the surface of the crystal, plotted in figure 5.4. The vertical displacement data shows that as we drag the indenter the crystal moves downwards with a total displacement of about 60μm, but when we analyse the groove surfece after scratching we see that the depth of the groove does not continuously increase. The continuous decrease in the vertical displacement might therefore be related to tilting of the top alumium plate as we drag the indenter. Even though we drag the indenter with a constant speed, the force measurement made by the load cell

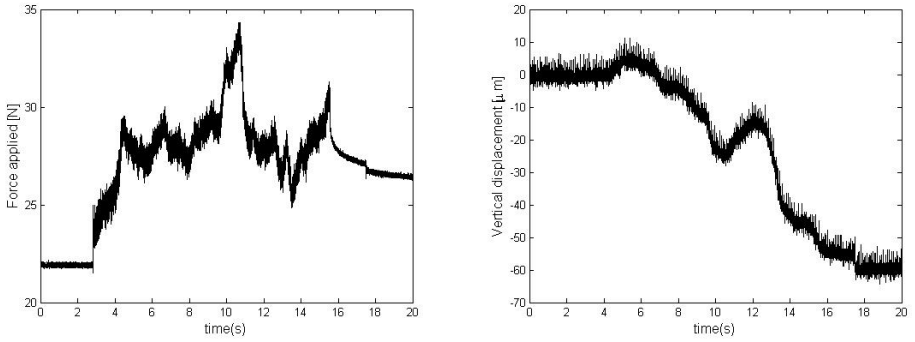

(a) force vs time (b) vertical vs horizontal time

Figure 5.4: (a) The force measured by the load cell plotted. We see small rise and drops in the force measurements that could be associated with stick slip motion.(b) Plot of horizontal displacement vs the time. We see that the crystal moves down as the glass bead scratches the bottom surface of the crystal.

have small rises and drops of up to 5N. The fact that the force builds up and then decreases again as we are moving the indenter can be caused by stick slip motion. The forces might be related to the braking of the crystal on the sides and creation of cracks at the edges of the groove.

Image of the crystal surface after indentation obtained with a white light interferometer is given in figure 5.5 (described in chapter 7). Interesting features we observe on the crystal surface after scratching is cracks at the edges of the groove going into the crystal, and triangular shaped breakage of the crystal on both sides of the groove. The cracks seem to have a preferentail orientation relative to the movement of the indenter, which is moving to the left in the picture. These type of patterns were also observed on the sliding surface of the crystal after a sandpaper experiment. When these cracks appear might be related to the rise and drops in the shear force mesurements (see figure 5.4a), but to check the relation between these two processes accurately is not possible with this data since the mechanical noise of the force measurement is too high.

In the rest of the chapter we will focus on the heat dissipation and analysis of the radiation signal monitored by the infrared camera. Now we will quantify the heat dissipated during the creation of this single groove.

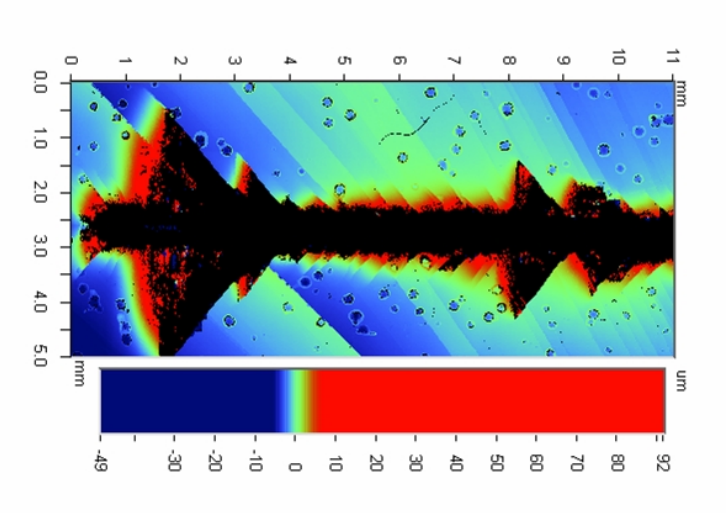

Figure 5.5: Image of the sliding surface of the crystal obtained by white light interferometer. The dark black region is the groove created by the indenter which is moving to the lft in the image.

5.3 Thermal imaging

5.3.1 Calibration

The bottom surface of the crystal is spray painted with black anti-reflective coating to eliminate the radiation noise from the background and to have a temperature indicator layer on the bottom of the crystal. The calibration technique we will use for the painted surface of the crystal is the same as used in the sandpaper and the peltier element case applied earlier. We decided to calibrate again the IR camera, since the experimental conditions are different now. Indeed, we will now observe with the infrared camera the bottom painted surface through the crystal. However we expect to obtain the same results as previous calibration (using the black coated surface of the peltier element) since the transmissivity of the halite crystal is equal to 92% within the range studied. We place a painted crystal on the peltier element with the crystals coated surface in contact with the peltier element. We make a scratch in the crystal to fit in the bead of a thermistor that is covered in thermal paste laying on the peltier element. The temperature of the peltier element is controlled by the PID program explained in the chapter 3. From calibrating the camera towards the painted surface of the peltier element, figure 3.10, we saw that the radiation signal and the temperature had a non-linear relation for large temperature differences. For a good linear

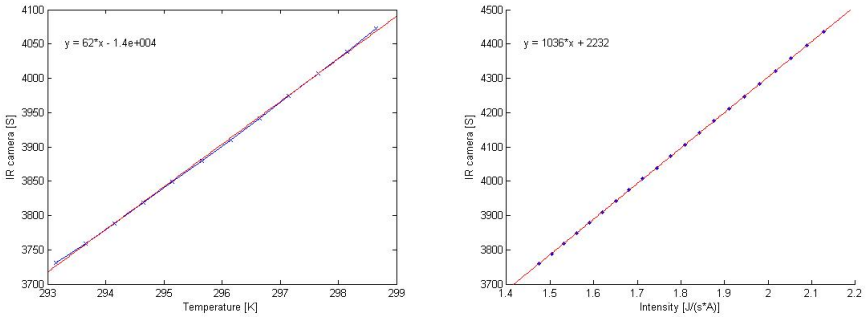

(a) IR vs Temperature (b) IR vs radiant excitance

Figure 5.6: (a) Plot showing the radiation signal measured by the infrared camera on the coated surface of the crystal and the equivalent temperature measured by the thermistor. The linear relation we get from these calibration is $A_{Temp} = 62$. (b) The radiation signal from the camera plotted against the theoretical radiation emitted by a blackbody in between 3-5μm for the same temperatures.

approximation between the radiation signal observed by the infrared camera and the temperature change at the bottom of the crystal we will calibrate the camera towards temperatures changes close to room temperature. The result of the calibration are given in figure 5.6. Using equation 3.3 we relate the temperature change with the radiation signal change

$$\Delta T = \frac{\Delta IR_{cam}}{\alpha}, \tag{5.1}$$

and the slope we get for the linear relation between these two is $\alpha = 62$. As discovered before when calibrating the camera to the peltier element and the sandpaper there is linear relationship between the theoretical radiation emitted by a blackbody between 3-5μm and the radiation signal measured by the infrared camera, described by equation 3.8. The slope for this linear relationship we get for calibrating the camera to the coated bottom surface of the crystal is $A_t = 1036$, which is very close to the calibration done to the coated surface of the peltier element $A_t = 1028$ (see figure 3.10b). The fact that the A_t is the same for both the coated surface of the peltier element and the coated bottom surface of the crystal means that when we look through the crystal the emissivity of the black anti-reflective coating is the dominating factor when lookin at the radiation signal change.

5.3.2 Experiment OS070

Now that we have calibrated the painted surface of the crystal we can again try to quantify the thermal dissipation. We run experiment OS070 at 1.7mm/sec and under the normal load of 3.4kg. Monitoring the radiation signal during this experiment we observe a large increase in the radiation at the indentation point, and once the indenter passes away the radiation drops down immediately as in the sandpaper experiments before. Since this signal measured by the camera can be due to the change of the topography of the surface with the creation of the groove, we can not be sure of a real increase of temperature at the tip of the groove. Therefore, we propose to analyse the radiation signal monitored by the infrared camera a bit away from the groove where no plastic and brittle deformation of the crystal is happening. Figure 5.7

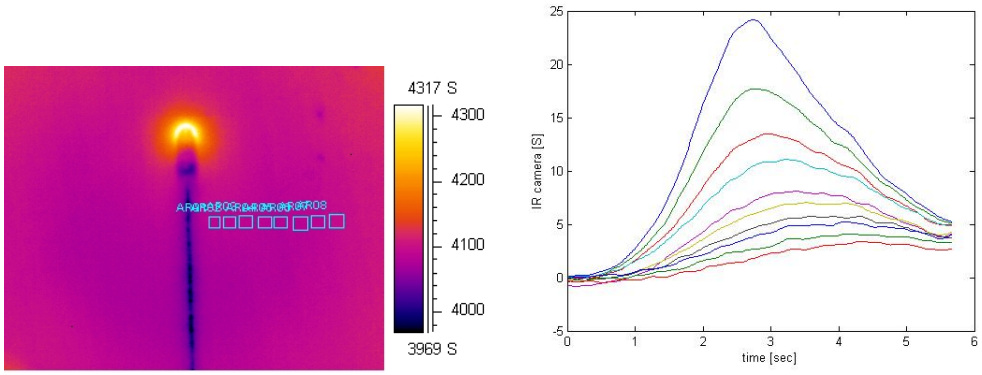

(a) IR image of OS070

(b) Radiation increase

Figure 5.7: (a) Infrared image of experiment OS70. The yellow bright spot in the middle is the indenter scratching the crystal and the rest is the bottom painted surface of the crystal.(b) The radiation signals monitored in small squares at a distance from the groove. Contrary to the sandpaper experiments we see a slow radiation decrease after the indenter passes as we would expect temperature to diffuse.

shows an infrared image of the scratching experiment, where the bright spot on the image is the indenter, and the image to the right shows the radiation changes that happens inside the boxes outlined in the infrared image, the boxes are only meant as indication of where the radiation is monitored. To the sides of the groove we observe slow increase in radiation and then a slow decreas, after the indentor has passed by, the maxima of the radiation curves get smaller as we go further away from the groove center, see figure 5.7. Con-

trary to previous experiments we can now link the signal measured by the camera to change of temperature at the surface of the crystal, by using the previous calibration.

Before doing this we are going to check directly if there is a temperature increase at the surface of the crystal by using a thermistor. Indeed, it could be possible that the increase in radiation signal comes from the radiation emitted by the glass bead and not from the paint.

5.3.3 Experiment OS72 with thermistor

To test this we placed the glass bead on the aluminium plate such that it would pass along about 3mm from the edge of the crystal. Advantage from this setup is that we can place a thermistor on the edge off the crystal and read directly out the temperature increase close to the groove. The thermistor is covered with thermal paste and made sure that it is only in contact with the crystal. Scratching the crystal with this setup and reading temperature change with the thermistor gives the increase shown in figure 5.8. The

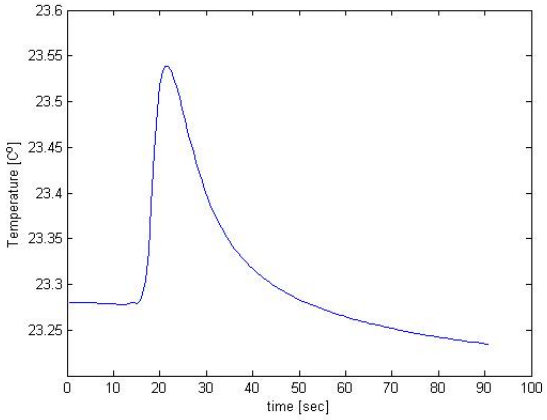

Figure 5.8: Temperature reading form a thermistor placed on the edge of the crystal and covered in thermal paste. We actually read temperature increase with the thermistor, meaning that we can be more confident in that the radiation changes monitored with the IR camera happen because of temperature increase.

total increase in temperature registered by the thermistor is $\Delta T_{incr} \approx 0.25°\text{C}$, and it happens within about 5 seconds and then the temperature decreases for approximately 30 seconds before reaching the initial temperature. The temperature continues to decrease even after reaching this point. This can

be explained by that when preparing the equipment for the experiment we touch the aluminium and the rig, which in turn increases their temperature relative to the surroundings.

Interpreting the radiation signal recorded by using the previous calibration we get the result shown in figure 5.9b. The left bright part of the infrared image shown in figure 5.9a is aluminum, and the small intrusion in the middle sticking out from under the aluminium is the glass bead. The increase and decrease pattern of the radiation we observe in this experiment is the same as that we observed in experiment OS070, with decreasing maxima as we go further away from the groove center.

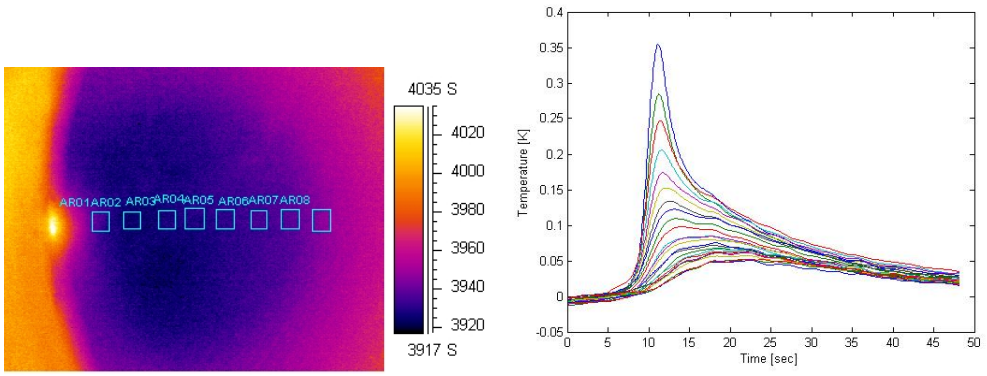

(a) IR image of OS72

(b) Radiation signals

Figure 5.9: (a) Infrared image of experiment OS072. The long bright area on the left side of the image is the top aluminium plate that the crystal is attached to, and the small yellow intrusion peaking out is the glass bead. (b) Average temperature signals in small square, a sketch of how these squares are places is shown in the infrared image to the left.

Now that we have clearly measured a temperature increase at the surface of the crystal during a sliding experiment we can now analyze in detail the radiation signal monitored by the camera during such experiments. This data analysis will be done in next chapter.

Chapter 6

Temperature analysis

6.1 Radiation reflections from the indenter

Before analyzing the radiation signal recorded by the camera as temperature let us analyse the signal and see how it behaves. Infrared image of experiment OS070 at time 3.98 is shown in figure 6.1, the size of the image is 8×10mm with a resolution of 256 pixels vertically and 320 pixels horizontally. The

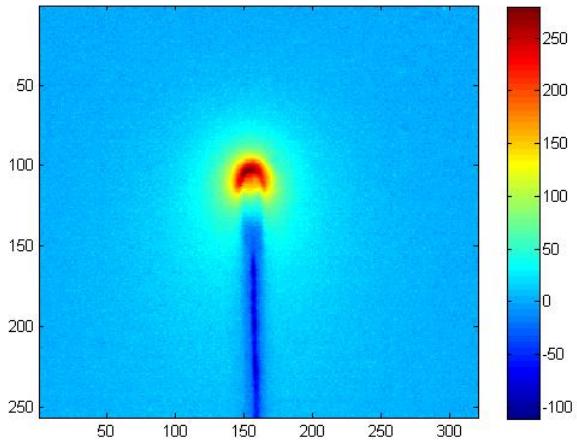

Figure 6.1: Infrared image taken at time 3.98. Te colorbar shows the radiation signal measured by the camera explained in chapter 3.4. The dark blue line is the groove and the red region is where the indenter is scratching at this particular time. The dimension of the image is 8×10mm

red spot in the middle is where the indenter is scratching the crystal, the

dark blue line behind it is the groove. We see that the tip of the groove is emitting more radiation than any other region, and the thick line that makes up the deformed groove is emitting less than any other area. To get a better view of the whole scratching process we average each picture vertically (i.e. in the direction the indenter moves) and collapse it into one vector of 320 values. Doing this for all 284 time steps and plotting the averaged vectors as a line gives the image shown in figure 6.2. The first top line in the figure

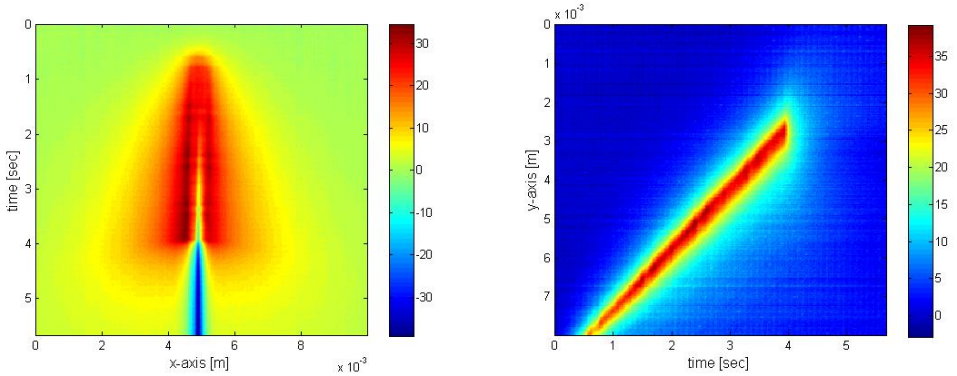

(a) averaged vertically (b) averaged horizontally

Figure 6.2: These images are created by the average of every infrared image at each time step, exactly how it is done is explained above.(a) This image shows how the radiation behind the indenter slowly decreases leaving a tail. (b) The red line in this image shows how fast the indenter is moving.

comes from collapsing the first image taken by the infrared camera at time $t = 0$s, and the bottom line comes from collapsing the last picture taken by the infrared camera at time $t = 5.66$s. The figure 6.2a shows how the radiation spreads out over time to the sides and how it makes a tail behind the indenter. Applying the same averaging technique in horizontal direction and reducing each infrared image to one vertical line gives the image shown in figure 6.2b. This red line in the image is telling where the indenter or the scratch tip is at one particular moment, and the angle of the red line is determined by how fast the indenter is moving. In figure 6.2b there is an abrupt reduction in the radiation as the indenter stops at time $t_{stop} \approx 4$s, this abrupt reduction might be an effect of that the radiation at the tip of the groove (indentation point)is so much higher that it makes it impossible to see the radiation changes other places in the image.

To see how much radiation that dies out when the indenter stops we take a line along the $y - axis$ with fixed position on the $x - axis$ for every time

step and make an image out of it. The first line we choose is at the center of the groove and gives out the image shown in figure 6.3a. As in image b shown above there is an abrupt reduction of radiation in this image also. Looking at a vertical line at a distance 0.72mm away from the center of the groove gives the image shown in figure 6.3b. Also in this image the radiation gets cut off as the indenter stops at about time t_{stop}. The line that we are looking at in the image is parallel to the movement of the indenter, therefore all the radiation monitored at this position must come from the paint or reflections inside the crystal of the indenter. The radiation that dies out with the movement of the indenter might be caused by reflections inside the crystal and not from thermal increase in radiation level of the paint. A bit below the area where there is an obvious cut off, $y > 4mm$, the radiations spreads out continuously even after the indenter has stopped. This means that this part of the radiation signal increase is related to heating of the crystal. To be sure of that we are reading of temperature variations at this position we must wait till about 1 second after the indenter has passed before interpreting the signal as temperature, or we must read of temperature after the indenter stops. To see how far these reflections from the indenter reaches we take a vertical line 1.7mm from the groove and a line 2.99mm from the groove and make the images shown in figure 6.3a and b. We still see a effect of the reflections 1.7mm away from the groove, but as we go further away to 2.99mm the effects are very small and we do not have an abrupt reduction in radiation. From the analysis of the images in figure 6.3 we can conclude that to be completely sure about that we are reading out temperature with the infrared camera we must look at a certain distance away from the groove, or wait till after the indenter has stopped or wait till it has moved a bit away.

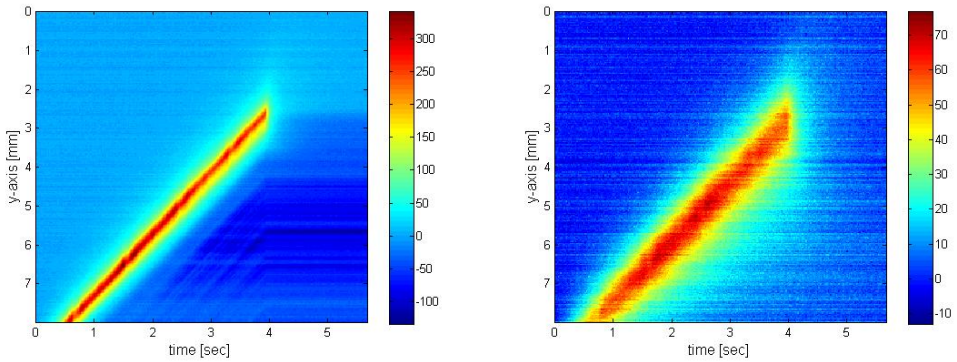

(a) groove center $\Delta x = 0$

(b) $\Delta x = 0.72mm$

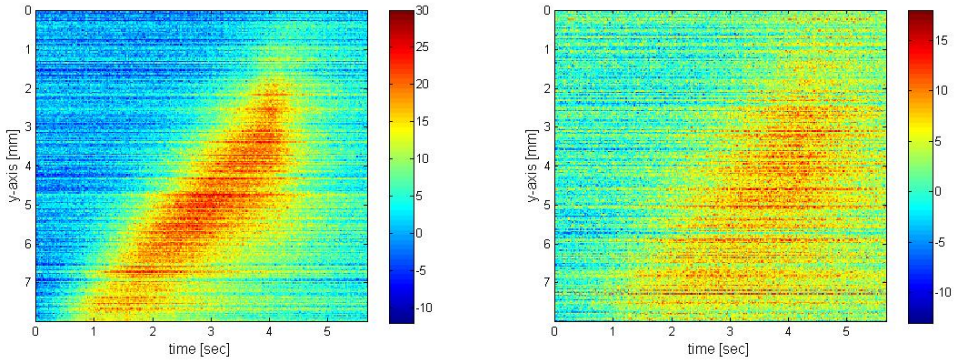

(c) $\Delta x = 1.7mm$

(d) $\Delta x = 2.99mm$

Figure 6.3: The images show the radiation change along a given position x. At the position of the groove we see an immediate decrease in radiation when the indenter stops. This immediate drop in radiation diminishes as we get further away from the groove until we see almost no effect in image d 2.99mm from the groove.

6.2 Thermal diffusion

Taking infrared imagery of the halite crystal during an friction experiment with the glass bead, gives us a two dimensional temperature profile around the indenter. Our objective further with this data is to give an estimate of how much energy is dissipated in heat. From this profile we can find out how much the surrounding of the groove at the interface between the paint and the crystal is warmed up. Giving an accurate estimate of the initial temperature increase of the system from this profile on the other hand is much more difficult. Because once the material that has gone through plastic

deformation or frictional heating is heated to its maximum temperature it will diffuse into the surroundings in all directions. To understand what part of this temperature increase we are reading of we must apply a solution off the diffusion differential equation to the data collected

$$\bigtriangledown (\lambda_c \bigtriangledown T) = \frac{\partial T}{\partial t} \rho C_p, \tag{6.1}$$

where λ_c is the conductivity, ρ is the density and C_p is the heat capacity. Boundary conditions we have in our experiment are an indenter deforming the crystal, leading to heating of the crystal, and there are four different materials involved in the diffusion process.

	λ [W/mK]	ρ [Kg/m^3]	C_p $[J/kg \cdot K]$
Aluminium	237	2700	897
Air	0.025	1.29	1012
Halite	1.5-10*	2.1-2.6$\cdot 10^3$	926
Glass	1.1	2600	840

The values in this table are taken from [12] . The dimensions of our setup seen from above and side are given in figure 6.4, the experiment we will be analysing in this chapter is OS072. The field of view we get from the infrared camera is 8×10mm, the groove length is l_g=23.3mm, the groove width is d_g=0.75mm, and the time it took to create it is Δt_g=13.7sec at a speed of v_g=1.7mm/sec. In an attempt to solve these equation 6.1 boundary conditions we will look into two different analytical solutions. We will start with comparing the data to a simple one dimensional analytical solution.

6.3 One dimensional heat source

The first solution we will compare the experimental result with is the classical point source solution [7]. In one dimension the boundary condition to this problem is

$$T(x, t=0) = \begin{cases} \delta(x) & \text{if } x = 0 \\ 0 & \text{otherwise} \end{cases}, \tag{6.2}$$

where $\delta(x)$ is the Dirac delta function, and $T = T_{measured} - T_{amb}$ is the temperature change following frictional heating by the indenter (T_{amb} is the ambient temperature). The solution of the differential equation 6.1 with these boundary condition is

$$T(x, t) = \frac{u}{\rho C_p \sqrt{(4\pi k t)}} e^{-x^2/4kt}, \tag{6.3}$$

* *Dale W.Kaufman* [18] and Crystran Ltd. suppliers of the halite crystal [14]

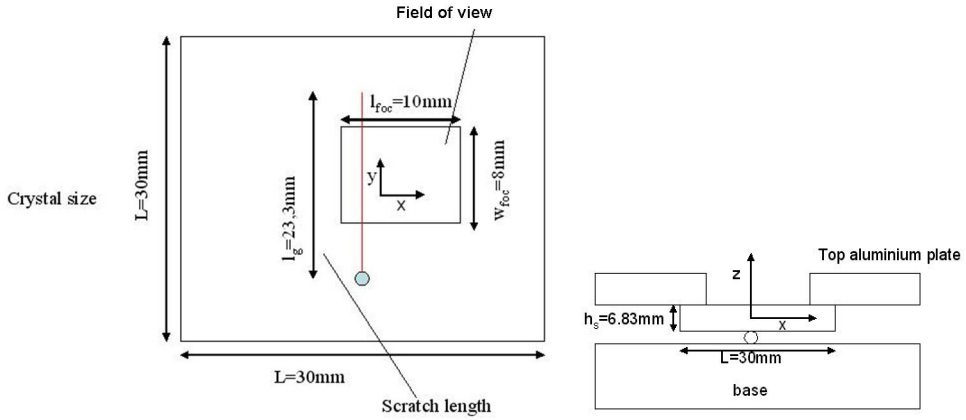

(a) xy plane (b) xz plane

Figure 6.4: Dimensions of the experimental setup in experiment OS072. (a) Top view of the crystal in xy plane. The final groove has the length l_g= 23.3mm scratched over a time period Δt_g=13.7sec at a speed of v_g=1.7mm/sec. (b) Side view of the experimental setup in xz plane. The height of the crystal is h_s=6.83mm and the distance between the base aluminium plate and the crystal about h_a ≈0.8mm

where $k = \frac{\lambda}{\rho C_p}$ diffusivity and u the thermal energy of the system. For us to be able to look at the process as one dimensional diffusion in x direction there are some conditions that have to be satisfied. The time the diffusion process is monitored $t \approx 40sec$ must be much larger than the time it takes to create the groove Δt_g=13.7sec and the distance measured at 1.6mm< x <8.5mm must be smaller than the length of the groove l_g=23.3mm. Also the height of the crystal h_s=6.83mm must be smaller than the distance measured at x and the heat diffused into air $J_{q,air}$ (heat flux) must be smaller than the heat diffused inside the crystal $J_{q,salt}$. The energy radiated $J_{q,radiated}$ must be smaller the energy diffused in the crystal because of convection $J_{q,salt}$. Summarizing the conditions that need to be satisfied in one dimensional case:

1. $t \gg \Delta t_g$
2. $x \ll l_g$
3. $x \gg h_s$
4. $J_{q,air} \ll J_{q,salt}$
5. $J_{q,radiated} \ll J_{q,salt}$

Condition 1 and 2 are satisfied, but 3 is not since the distance we are measuring at is for the most part smaller than h_s and we can not look further away cause the signal would be to small and get overshadowed by the

noise. The condition nr. 4 is also satisfied since the conductivity of the air $\lambda_{air} = 0.025W/mK$ is much smaller than the conductivity of the halite crystal $\lambda_{salt} = 6.5W/mK$. The last condition is satisfied for the halite crystal since the emissivity of the halite crystal is very small (see chapter 3).

Even though not all of the conditions are satisfied we will see how well the point source solution in one dimension compares to the experimental data. Using the variable $\eta = \frac{x}{\sqrt{4t}}$ equation 6.3 can be rewritten as

$$x \cdot T = \frac{A\eta}{\sqrt{k}} e^{-\frac{\eta^2}{k}}, \tag{6.4}$$

where $A = \frac{u}{\rho C_p \sqrt{\pi}}$ is a constant. From this equation we can see that all curves of $x \cdot T\,(x,t)$ plotted against η should fall on a single line. Derivating it with respect to η gives

$$\frac{\partial x \cdot T}{\partial \eta} = \frac{A}{\sqrt{k}} \left(1 - \frac{2\eta^2}{k}\right) e^{-\frac{\eta^2}{k}}, \tag{6.5}$$

and setting it equal to 0 tells us that the maximum for all curves should occur

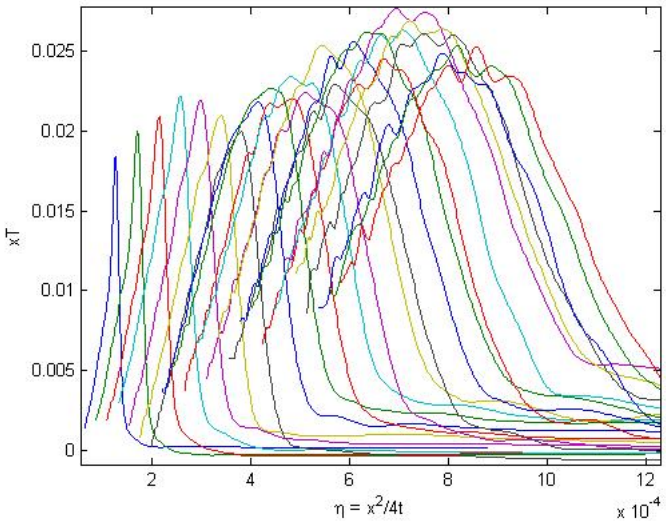

Figure 6.5: Attempting to collapse the data on a single line to check whether the one dimensional point source solution to the thermal diffusion equation can be used as an comparison to the observed diffusion process in experiment OS072. The different curves are the temperature evolution at different positions x.

a $\eta = \sqrt{\frac{k}{2}}$ and have the value $x \cdot T_{max} = \frac{A}{2} e^{-\frac{1}{2}}$. So if all the experimental data

collapse on the curve $\frac{A\eta}{\sqrt{k}}e^{-\frac{\eta^2}{k}}$ the source point solution can be used as good estimate of the total thermal energy generated during the experiment. Taking the smoothed data from experiment OS072 (see figure 5.9) and plotting $\eta = \frac{x}{\sqrt{4t}}$ against $x \cdot T(x,t)$ gives the result shown in figure 6.5. The distance x is measured from the center of the groove and t is the time the temperature differences are monitored with the infrared camera.

As seen in the figure the curves do not collapse perfectly on top of each other. The first curves are very narrow with steep increase and decrease, while the last curves are much wider with slow increase and decrease in $x \cdot T$. One reason for this can be that condition 3 is too important to neglect. Another explanation might be that experiment OS072 had the indenter moving at the edge of the crystal and the crystal was attached to the top aluminium plate right above the scratch. Because of this the aluminium which is much better thermal conductor than the crystal might be leading off to much heat away and hence complicating the boundary conditions.

6.4 Two dimensional heat source

Considering that a one dimensional solution was not a good comparison to the experimental data we will try a two dimensional analytical solution in xz plane. The fact that in experiment OS072 the indenter scratched at the edge of the crystal complicates the diffusion process, therefore we return back to experiment OS070 where we scratch in the middle of the crystal.

Before trying to fit a solution of the diffusion differential equation lets take a look at how the radiation signal behaves at the interface between paint and crystal. In the experiments the infrared camera is focused on the painted surface of the crystal which is held still, the indenter is the moving object that comes from the bottom of the image, see figure 5.7. It so passes through the field of view of the camera scratching up the sliding surface of the crystal. In experiment OS070 we stopped the indenter before it left the field of view and then let the surroundings cool down before we continued moving it. Looking at the temperature changes as the indenter comes inside the image gives the result shown in figure 6.6a for different time steps. The curves given in the figure are the vertical average of the bottom 56 pixels in the infrared image (equivalent of 1.7mm or about 1/4 of the image). We take the bottom of the picture since the indenter enters from the bottom and manages to pass away from this region before we stop it. An important thing to note in this profile is that the area under the curves are diminishing for each time step. In the one dimensional solution the heat can only travel in the x-direction and since the energy is conserved the area under the temperature curves must

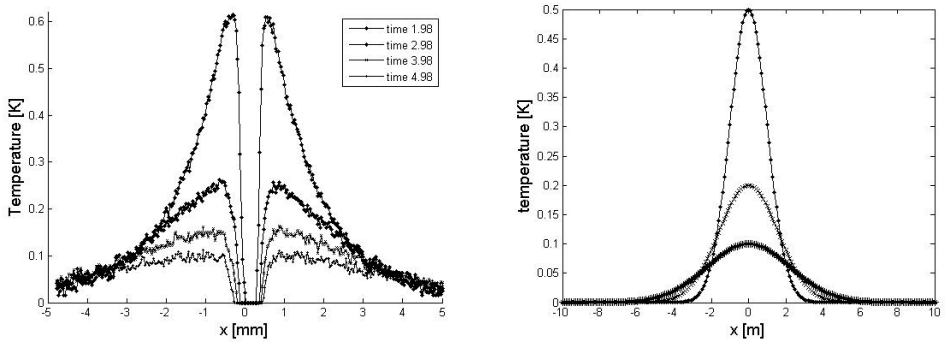

(a) Experiment OS070 (b) Analytical 2D solution

Figure 6.6: (a) Plotting the temperature evolution as observed by the infraread camera for different time steps. The middle of the curves are set to zero, since that is where the indenter scratches. The area under the curves diminishes, meaning that heat is being transferred up in the crystal. (b) Plotting the analytical solution of the 2D point source solution for different time steps. Also in this process we see decrease in the net area under the temperature curves.

be constant. This discrepancy between the experimental diffusion process and the one dimensional solution shows that they are not the same diffusion processes.

The two dimensional solution we will compare the experiments to is the point source heating in a 2D half space. The boundary conditions for this solution are almost the same as in the one dimensional point source case, only difference being that we now have two dimensions.

$$T\left(x,z,t=0\right)=\begin{cases}\delta\left(x\right)\delta\left(z\right) & \text{for } x=0\\ 0 & \text{for z>0 and x}\neq 0\end{cases} \tag{6.6}$$

The solution of the differential equation for these boundary conditions is [7]

$$T\left(x,z,t\right)=\frac{A'}{2\pi kt}e^{-\left(x^2+z^2\right)/4kt}. \tag{6.7}$$

The conditions that have to be satisfied for this solution to be valid are that the diffusion must only happen inside the salt crystal, $J_{q,air}\ll J_{q,salt}$. As in the one dimensional case the the monitoring time $t\approx 5.6sec$ must be greater than the time it takes to create the groove $\Delta t_g=3.5sec$, the distances measured at $1.6mm<x<5mm$ must be smaller than the distance to the ends of the groove of the groove $l_g=6.5mm$, and the radiated energy $J_{q,radiated}$

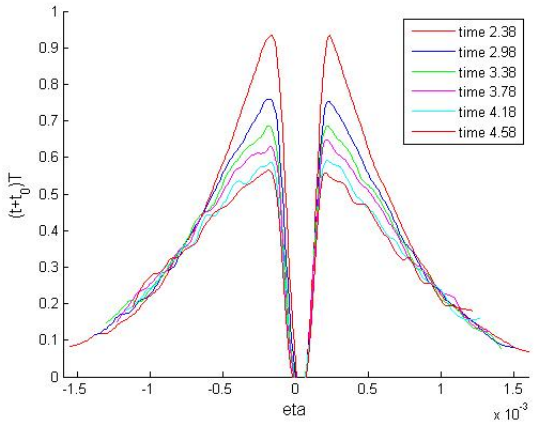

Figure 6.7: The time multiplied by the temperature plotted against $\eta = \frac{r}{\sqrt{4t}}$. According to equation 6.8 the curves should collapse on each other, but as seen in the plot the curves get broader as the time progresses.

must be smaller than that diffused inside the crystal $J_{q,salt}$. Summarizing these conditions:

1. $t \gg \Delta t_g$
2. $x \ll l_g$
3. $J_{q,air} \ll J_{q,salt}$
4. $J_{q,radiated} \ll J_{q,salt}$

All of these conditions are satisfied, although condition 1 and 2 are at the limiting edge. To check how this equation behaves at position $z = 0$ over time, we set $\frac{A'}{2k} = 1$, $\frac{1}{4k} = 1$ and plot $T(x, z = 0, t) = \frac{1}{t}e^{-x^2/t}$ for three different times see figure 6.6b. As in the experiments we see in the figure that the area under the temperature curves along x, $z = 0$ diminishes. Since the solution passes the first test we will again try to collapse the experimental data according to the 2D point source solution.

6.4.1 Collapsing the data to 2D solution

In order to collapse the data we again make use of the variable $\eta = \frac{r}{\sqrt{4t}}$ ($r^2 = x^2 + z^2$) and transform equation 6.7 into

$$t \cdot T(x, z, t) = \frac{A}{k}e^{\eta^2}, \quad A = \frac{A'}{2\pi} \tag{6.8}$$

The smoothed temperature data from the experiment multiplied by the time, $t \cdot T$, is plotted against η in figure 6.7. We see in the figure that the curves

maximum values are decreasing and the curves get broader as the time increases.

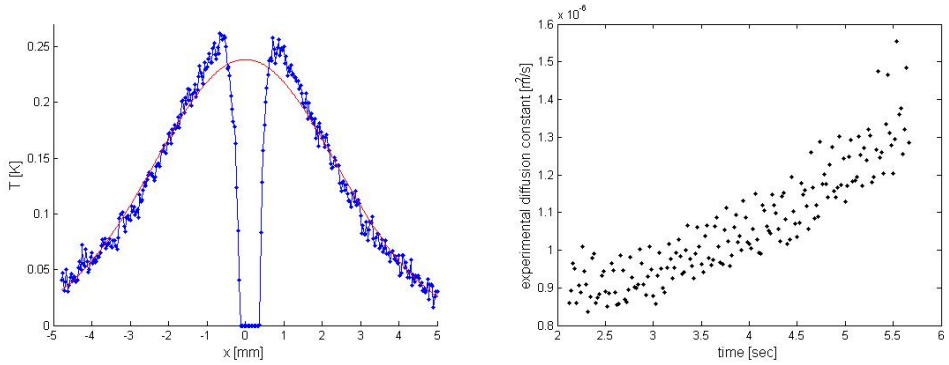

(a) Time step 150 (b) Diffusion constant

Figure 6.8: (a) Plot showing the raw experimental data at time $t = 2.98$ and the fit of equation 6.7 to the data. The data in the middle is not taken into account when fitting the curve, since that is where the indenter scratches the crystal. (b) We see a linear increase in the diffusion constant, calculated from the fitted curves for each time step an infrared image is recorded.

To investigate this effect more thoroughly we try fitting the experimental data to equation 6.7 and see how the parameters vary. We reduce the equation into linear form

$$\log(T) = \log\left(\frac{A}{(t-t_0)\,k}\right) - \frac{1}{4k\,(t-t_0)} \cdot r^2 = a - b \cdot r^2, \qquad (6.9)$$

and use the least square method determine the unknown parameters. The parameters that need to be determined are then a and b, t_0 is the start time of the process and set to zero for now. We ignore the points in the middle of the curve when fitting equation 6.9 to the experimental data, since the thermal signal there is overshadowed by the emissivity changes. How the fitting works for time step 150, that is $time = 2.98$sec is shown in figure 6.8a, and the parameters we get out for this particular time step are $a = 8.84 \cdot 10^4$ and $b = -1.43$. Translating the constant b back into the diffusion constant using the relation $k = \frac{1}{4b(t-t_0)}$, gives the distribution of the diffusion constant for each time step as shown in figure 6.8b. We see in the figure that there is a trend in the diffusion constant, it increases with time. This trend in the diffusion constant might be caused by that the start time t_0 has not been correctly adjusted for. So far the time has been counted from the moment

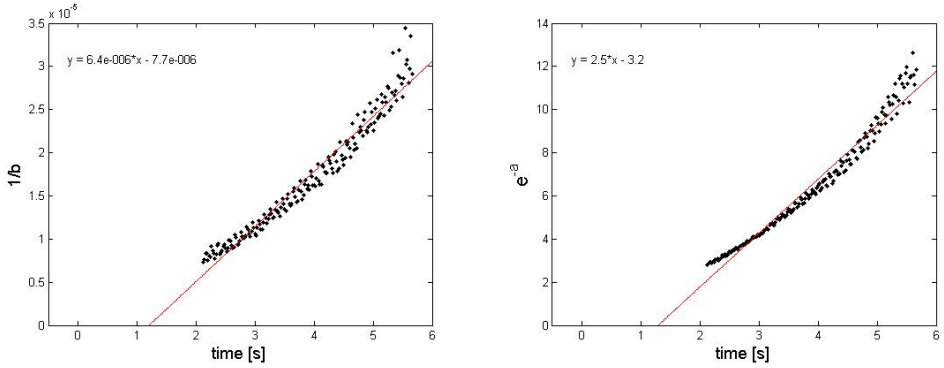

(a) relation 1 (b) relation 2

Figure 6.9: (a) The start time t_0 is estimated by finding out where the linear fit to the time t plotted against the parameter $\frac{1}{b}$ intersects the $x-axis$. (b) A second estimate of the start time is obtained by finding out where the linear fit to time against e^{-a} intersects the $x-axis$.

the infrared camera started measuring. To get a more correct estimate for the start time t_0 we look at the fitting parameters

$$b = \frac{1}{4k\,(t - t_0)}, \tag{6.10}$$

$$a = \log\left(\frac{A}{(t - t_0)\,k}\right). \tag{6.11}$$

Rewriting these two equations with the time on the left side gives

$$t - t_0 = \frac{1}{4kb}, \tag{6.12}$$

$$t - t_0 = \frac{A}{e^a k}. \tag{6.13}$$

From these equations we see that there is a linear relation between the time $t - t_0$ and the parameter $1/b$. This linear relation between the time and the fitting parameters requires that the line given by equation 6.12 intersects the $x - axis$ at time t_0. The estimate we get out for t_0 from this relation is the actual start time of the diffusion process, and the time t should be corrected for this start time. There is also a linear relation between e^{-a} and $t - t_0$ given by equation 6.13, and for this case as well the line given by the linear relation should intersect the x-axis at time t_0. Plotting the time against $1/b$ (see figure 6.9) and fitting a linear equation $y = c \cdot xd$ gives $c = 6.4 \cdot 10^{-6}$ and

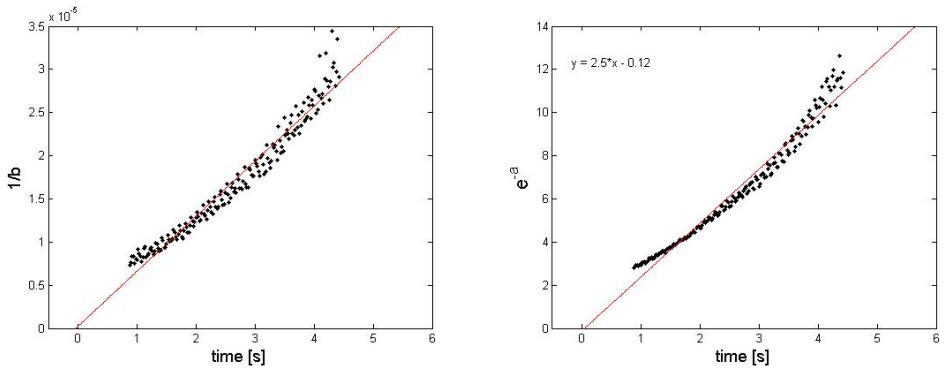

(a) relation 1 (b) relation 2

Figure 6.10: The fitting parameters e^{-a} and $1/b$ plotted against the adjusted time. We see that the linear fit to these data intersects the $x-axis$ at $t=0$

$d = 7.7 \cdot 10^{-6}$, which in return gives $t_0 = 1.2$s. For the relation between time and e^{-a} we get $c = 2.5$, $d = 3.2 \cdot 10^{-6}$ and $t_0 = 1.3$s, see figure 6.9b. Now that we have estimates on the start time of the diffusion process we adjust the time in the experiments by the average of the start times gotten from the relations above, $t_{0,av} = 1.25$s. Plotting the relations given by equation 6.13 and equation 6.12 again with the adjusted time gives the result shown in figure 6.10. As seen in the figure the fitted lines to the data now intersects very close to time $t = 0$, neither of them intersects exactly at 0 since we took the average of both of them when estimating t_0. Now that we have corrected for the actual start time of the diffusion process we again try collapsing the data on one single curve given by equation 6.8, the result of this collapse for 6 different times is given in figure 6.11. As seen in the figure the collapse is much better than in figure 6.8. Even though the curves do not perfectly land upon each other, they are close enough to call this model a good fit for the experimental data. The variation in the diffusion constant calculated from equation 6.10 for each time step is given in figure 6.11b. There is no longer an increasing trend in the diffusion constant as was observed in figure 6.8b. The best estimate of the diffusion constant from the slope in figure 6.10a is $k = 1.6 \cdot 10^{-6} m^2/s$. Literature values for the diffusion constant k of NaCl vary between $0.77 - 5.1 \cdot 10^{-6} m^2/s$, the diffusion constant we get is within this range.

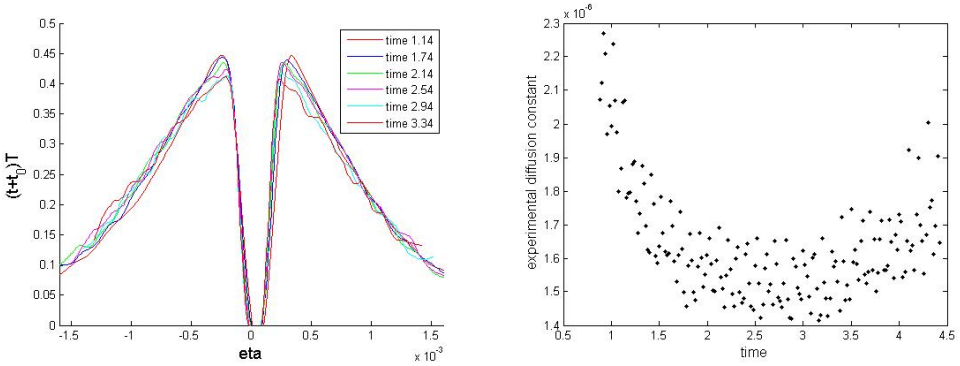

(a) collapsed curves

(b) diffusion constant

Figure 6.11: (a) Plotting $t \cdot T$ against η for the same time steps as in figure 6.7 with the adjusted time, collapses the curves very well. (b) The diffusion constant is estimated by fitting the equation 6.7 to the raw data. Adjusting the time from the equations 6.13 and 6.12 removes the linear increase observed in figure 6.8b.

6.5 Estimating the thermal energy

The work done scratching the crystal is given by the amount of force applied to drag the indenter times the distance. The force measured in experiment OS072 by the load cell is given in figure 6.12. Since the force increases rapidly for the first 1 mm of the dragging distance, we average over the force from 1mm and onwards to 6mm where it has a fairly steady value, $F_{av} = 31.82N$ with the standard deviation of $\sigma_{F_{av}} = 1.21N$. The amount of work spent moving the indenter for 5 mm is then

$$W_{tot} = F_{av}\Delta l = 0.16J$$

The two dimensional point source solution describes the temperature distribution of a cross section of the crystal in xz-plane. While the energy generated by temperature differences in a material is given by

$$u = \rho V C_p \Delta T, \tag{6.14}$$

where V is the volume, C_p is the heat capacity and ΔT is the change in temperature. To get the energy for a volume of the crystal we will have to integrate equation 6.7 for a half space in all three spatial directions, (x, y, z).

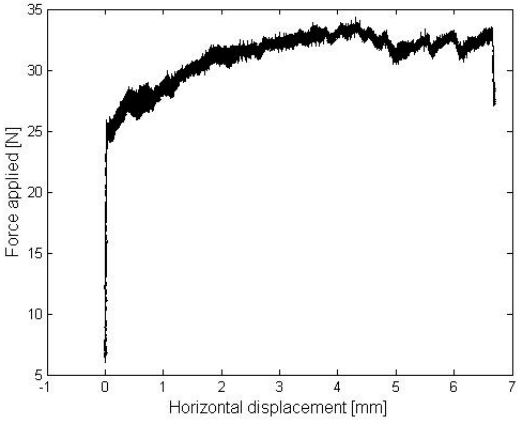

Figure 6.12: The force measured by the load cell plotted against the horizontal displacement.

Since the indenter is moving with the same speed and shear force in y direction the thermal energy generated in this direction is also constant. Considering that the temperature is diffusing in a half space we formulate the integral in polar coordinates

$$u = \int_0^{\Delta l} \int_0^{\pi} \int_0^{\infty} \rho C_p T(r,\theta)\, r dr d\theta dy. \tag{6.15}$$

The integral in y direction is taken for the same length as the work is estimated for $\Delta l = 5mm$ and θ is integrated from 0 to π because the solution is only for a half space. The distance r is integrated from 0 to infinity, since the temperatures approaches zero at the boundaries of the crystal. Setting in the equation for T and integrating gives

$$u = \int_0^{\Delta l} \int_0^{\pi} \int_0^{\infty} \rho C_p \frac{A'}{2\pi kt} e^{-r^2/4kt} r dr d\theta dy = \rho C_p \Delta l A'. \tag{6.16}$$

Putting this result back in equation 6.7 we get the final result that we can estimate the thermal energy from

$$T(r,t) = \frac{u}{2\rho C_p \Delta l \pi kt} e^{-r^2/4kt}. \tag{6.17}$$

To estimate the energy u in the above equation we fit this equation to the experimental data like before and determine it from the fitting parameter a in equation 6.9. The heat capacity for halite crystal is $C_p = 926\ [J/kg \cdot K]$

and the density is $\rho = 2160$ Kg/m^3. The thermal diffusivity used to estimate the thermal energy is calculated from the fitting parameter b in equation 6.12 (see figure 6.10a) for each timestep. The result we get for the estimate of the thermal energy is shown in figure 6.13. The mean value we get for the thermal energy is $u_{mean} = 4.15 \cdot 10^{-}2$ J with a standard deviation of $u_{std} = 3.2 \cdot 10^{-}3$ J.

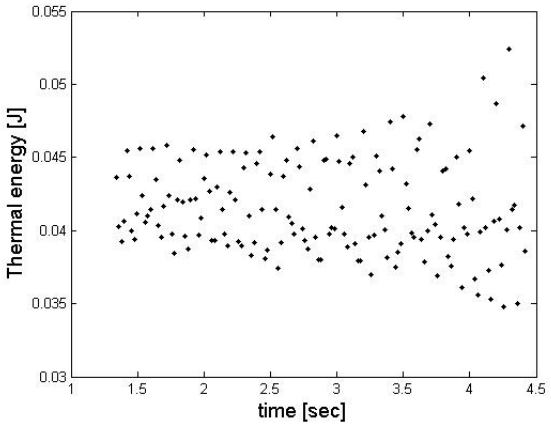

Figure 6.13: The thermal energy estimated by fitting the equation 6.17 to the raw experimental data.

The thermal energy makes up a fraction 0.26 of the total work applied at moving the indenter and the aluminium plate it is attached to. This fraction might be higher if the work that needs to be applied to resist the friction of the rig when moving the indenter had been subtracted from the normal force measured by the load cell. Estimating the force needed to resist the friction is not possible right now, since the rig has been dismantled to reduce this exact friction.

Chapter 7

Surface analysis

We use a white light interferometer For surface analysis of the sliding surface of the crystal. The interferometer gives a three dimensional surface profile of the crystal like shown in figure 7.1a. The first surface we investigate is of a crystal that has been scratched under the normal load of 3.38kg and velocity 1.7mm/s (experiment A). In the image the glass bead is sliding from top to bottom, and the dark area in the middle is the centre of the groove, the interferometer is not able to resolve the surface profile of this area at this magnification because of steep angles. An interesting feature we observe on the crystal surface after scratching is cracks at the edges of the groove going into the crystal. As the crystal scratches the surface it also breaks of chunks of the crystal at the edges, usually making a triangular shapes as seen in figure 7.1a. The angle these chunks make with the movement direction of the indenter seem to be determined by the already existing structure planes in the crystal. These planes in the image can be seen as the lines going from higher point at the right side to a lower point on the left side. Although the cracks seem to be determined by the crystals structure on the left side of the groove, they move almost normal to the structural planes of the crystal on the right side of the groove.

To check how dependent the formation of these cracks is to the internal structure of the crystal, we run experiment B with the indenter moving normal to the planes in the crystal, normal load and sliding velocity are kept the same. The result we get from this experiment B is shown in figure 7.1b. As seen in the image the cracks are much smaller than in experiment B and they do not have the same preferential angle as observed in previous experiment. The differences in the crack orientation and the amount of crystal that is broken of at the sides of the grooves between experiment A and B, shows that the formation of the cracks is related to the structure of the crystal and dependent on the relative movement of the indenter to the crystal plane.

One thing to note about both of these experiments is that the crystals have been recrystallizing for about 5 months before the topographic profiles are extracted.

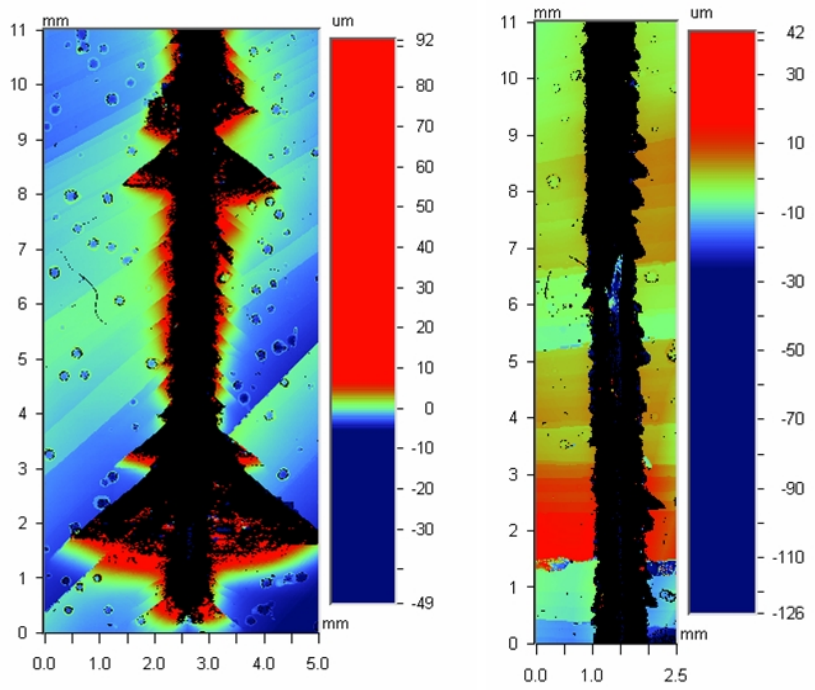

(a) Experiment A

(b) Experiment B

Figure 7.1: Images of the topography of the sliding surfaces of the crystals used in experiment A and B, the indentor is moving downwards in the images for both of them. (a) The groove in the middle is not resolved into heights by the interferometer because of very steep angles inside the groove. At the edges of the groove the crystal is pushed up higher creating pil-ups. (b) Experiment B was conducted such that the indenter moved normal to the already existing planes in the crystal. We see that this effect the amount of damage that is done on the sides of the crystal.

7.1 Surface energy

For better analysis of the surface deformation inside the groove we measure the surface profile with greater magnifications. Figure 7.2 shows images taken

with the white light interferometer of the groove created in experiment B, we take this images in between approximately 5 and 7mm in figure 7.1b.

The top image in figure 7.2 shows that the surface is higher at the edges of the groove than at the flat undeformed surface on the sides. This material has been pushed up by the indenter as it scratches the crystal making pile-ups on the sides of it. When we come inside the groove past the pile-ups the surface height decreases in an elliptical shape (see figure 7.3). One reason for showing this particular image is that in the middle of the groove there is a flat surface with the same height as that of the undeformed surface on the edges of the image. This area is only about 1mm long, but considering that it is in the middle of the groove it is still a very unexpected surface feature. We do not observe any such feature in experiment A or any other place along the scratch line of crystal B. Zooming in further at the edge of the groove shows that the crystal is highly deformed with height variation of up to 115μm in an area of 186×248mm. To see how crushed the crystal surface inside the

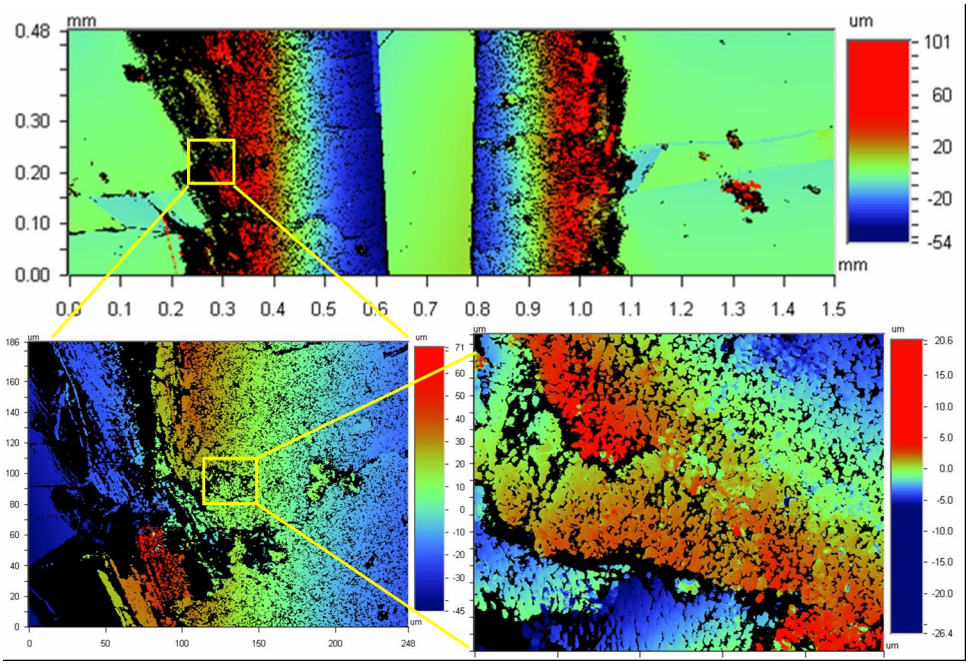

Figure 7.2: Surface profiles of experiment B with different magnifications. The first image gives an overview of the topography, showing pile-ups at the edges and the height decrease inside the groove. The dimensions of the last image is 45×60μm, and we observe from it that there is still lot of height variation in such a small region, indicating crushing of the crystal into small grains.

groove is we zoom further in and get the surface profile shown in the last image in in figure 7.2, the dimensions of the image is 45×60μm. From this magnification we observe that the surface of the crystal has been crushed into grains of about 3μm in diameters.

7.1.1 An upper estimation of the surface energy

The damage done to the crystal decreases as we go away from the groove surface, until the edge of the plastically deformed region beyond where there is no deformation. Therefore the crystal is broken into smaller pieces at the surface of the groove and as we get closer to the undeformed region the cracks going into the crystal widen up creating less amount of new surface. For an upper estimate of the energy needed to produce new surface in the plastically deformed region of the crystal, we assume that the damage done in the whole deformed region is the same as that observed on the surface of the groove.

We approximate the shape of the deformed crystal grains observed on the surface of the groove as cubes with the dimensions $l = w = h = 3\mu$m, the total surface area of the cube is then

$$A_{cube} = 6 \times l^2 = 54\mu m^2.$$

We assume that the whole plastically deformed region is divided into these cubes. Looking at the surface profile of experiment B at a place where the whole groove is deformed and not where we have the anomaly shown in figure 7.2, and averaging the surface profiles in y direction for about 0.29mm we get the surface shape in xz-plane shown in figure 7.3a. Since the upper surface of the groove is shaped as an ellipse (see figure 7.3), we approximate the deformed area under the surface to be shaped as an ellipse too. Ignoring the pileups at the edges, the area of the deformed region in xz plane can be written as

$$A_{def} = \frac{\pi}{2}(a_c + a_s)(b_c + b_s) - \frac{\pi}{2}a_c b_c, \tag{7.1}$$

where a_c, b_c, a_s and b_s are the spatial dimensions explained in figure 7.3b. From the topography profile analysis we see a slope in the surface for about 2.5mm from the center of the groove, and the width of the groove is about 1mm (a_c = 0.5mm), and the depth is approximately $b_c = 40\mu m$. The dimensions of the plastically deformed region is then $a_s = b_s = 1.5mm$. Using these approximations we get the total volume of the deformed region for a groove of length $\Delta l = 1.3cm$

$$V_{tot} = A_{def} \cdot \Delta l \approx 62mm^3,$$

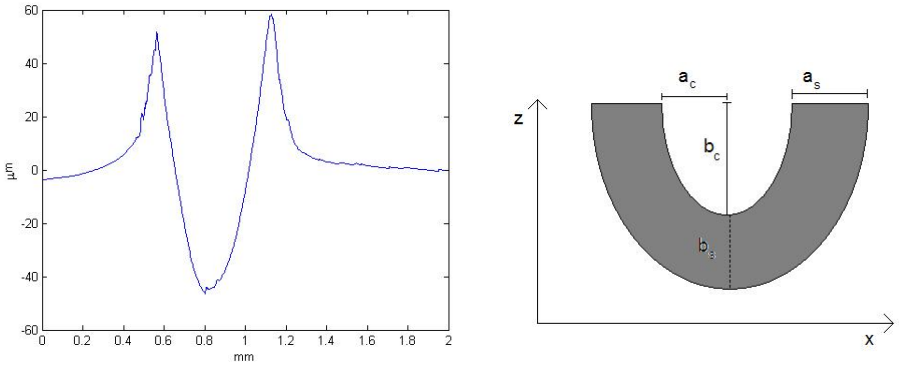

(a) Experiment B

(b) Spatial sketch

Figure 7.3: (a) The profile of the groove in $xz - plane$, it has been averaged over a distance of 0.29 mm along the movement of the indenter ($y - plane$). The tops on the edges of the groove are the characteristic pile-ups observed in scratch tests. (b) A sketch showing how we approximate the shape of the grooves an ellipse, the grey area is the plastically deformed region.

and the amount of grain cubes inside this volume are

$$n = \frac{V_{tot}}{l^3} \approx 2.3 \cdot 10^9.$$

The total surface surface area for all the cubes is

$$A_{tot} = nA_{cube} \approx 1.25 \cdot 10^{-1} m^2,$$

An upper estimation of the surface energy of halite is $\gamma_{NaCl} = 0.37 J/m^2$ [27], the total energy spent producing new surface area is then

$$W_{surf} = \gamma_{NaCl} A_{tot} \approx 4.62 \cdot 10^{-2} J.$$

7.2 The total work

The force measured in this experiment by the load cell is plotted against the movement of the indenter in figure 7.4. As seen in the figure the force applied at dragging the indenter is fairly stable between position 0.5cm to 1.8cm. For estimating the work done in this distance $\Delta l = 1.3cm$ we use the mean force $F_{av} = 29$ N and get

$$\overline{W}_{tot} = F_{av} \Delta l = 29N \cdot 1.3 \cdot 10^{-2} m = 37.7 \cdot 10^{-2} J.$$

According to the upper estimation of the energy spent producing new surface area in this experiment, out of the total work that is applied at moving the indenter and the base (the bottom aluminium plate it is attached to) 12.25% goes to producing new surface. As discussed in previous chapter when estimating the thermal energy dissipated in the experiments, the total work that is applied does not all transfer into the deformation of the crystal. A small part of it is used to resist the friction of the rig that is dragging the indenter, and it is now not possible to estimate how much this friction is because the rig is dismantled, and the whole experimental setup is being changed into something that has less frictional and mechanical noise in it.

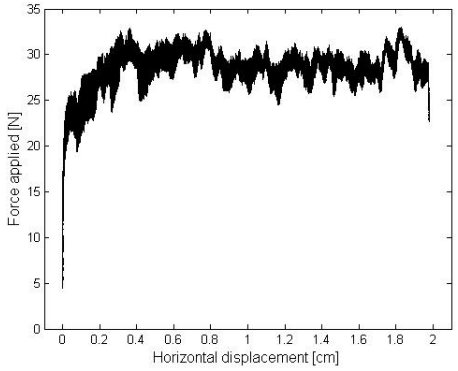

Figure 7.4: The force measured by the load cell in experiment B plotted against the horizontal displacement of the indenter.

Chapter 8

Conclusion and perspectives

Although calibration of the infarered camera for estimating temperature change from radiation monitored has been performed. Carefull calibration of the heating of the camera, the optics, and the radiation signal for large temperature changes is conducted to lay the foundation for quantative use of the IR camera in the dissipation study that followed.

Sliding friction experiments simulating a fault system by dragging a sandpaper on a halite crystal were conducted to check wether it was possible to estimate the heat production and diffusion from the radiation signal measured by an infrared camera. The radiation changes caused by the evolution of the topography of the crystal surface due to the formation of the groove by brittle and plastic deformation are really important. Therefore it is impossible to measure accurately an increase of temperature exactly at the position where the groove is created, since we are not able to distinguish emissivity changes and thermal processes.

Therefore, we proposed to simplify the first experimental setup using sandpaper for scratching the crystal by developing experiments with only a single indenter (glass bead) deforming the crystal surface. This configuration makes it easier to characterize and quantify the mechanical behaviour and the thermal increase in the crystal during frictional sliding experiments. Indeed, using a single indenter concentrates stresses locally and creates a single groove, bigger and deeper than the ones formed using sandpaper (the sandgrains are smaller,and the stress is redistributed over all the contact points); and therefore the heat dissipated in that case is also expected to be larger. Then, monitoring the radiation signals with an infrared camera at the coated bottom surface of the crystal, a bit away from the groove where no surface deformation is happening allows us to convert the radiation change recorded into temperature change. To estimate the thermal energy generated in experiment OS070 we used the two dimensional point source solution in a half

space (only considering the salt) to determine the total energy dissipated in heat. From this estimation we found that the mean thermal energy produced in this experiment was $u_{mean} = 4.15 \cdot 10^{-2} J$, which made up 26% of the total work applied at moving the indenter (and the base).

Investigating the surface of the crystals after they have been scratched with a white light interferometer showed that the crack and breakage of the crystal on the sides of the grooves was related to the relative movement direction of the indenter and the already existing structural planes of the crystal. Looking with higher magnification ($\times 100$) at the surface of the grooves we discovered that the surface of the groove was divided into grains of particular size. From this breakage pattern at the surface of the grooves we made a upper estimation of the energy spent on producing new surface area in the plastically deformed region around the groove, $W_{surf} = 4.62 \cdot 10^{-2}$ which makes up 12.25% of the total work applied at dragging the indenter (and the base).

In this work, we focused on estimating quantitatively a local increase of temperature during a friction process. However we observe that the mechanical behaviour is rich and complex even when we just drag a single indenter at the surface of the crystal see figure 8. Indeed the force measured during such experiments is characterized by an intermittent behaviour with sudden jumps and drops of various amplitudes. This might correspond to the complex topography of the groove, characterized by cracks on the sides of the groove, and wavy patterns at the bottom of the groove itself. Moreover this complex dynamics can be studied in more detail by recording simultaneously the force and the acoustic emissions (using wide band sensors in the ultrasonic range) during the sliding experiment. Such preliminary experiment is presented in figure 8 and will be subject of future investigation.

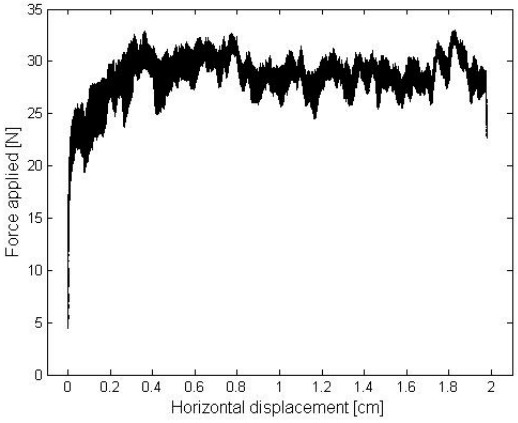

(a) force

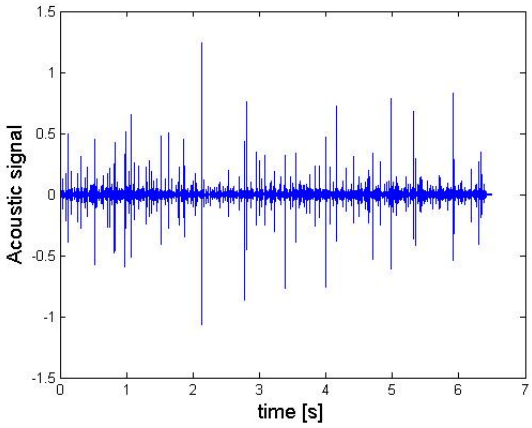

(b) Acoustic data recorded during same experiment

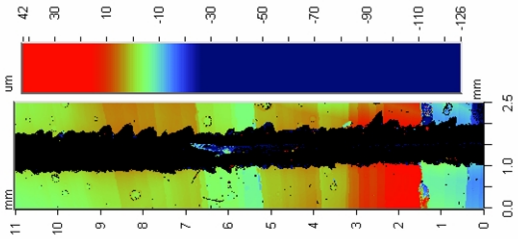

(c) topography of the groove obtained by white light interferometry

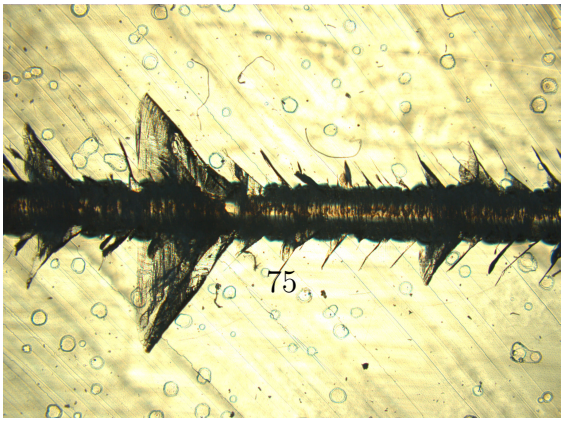

(d) image of a groove obtained with a microscope, the scale is 8mm×5mm

Appendix A

Optical property of sodium chloride

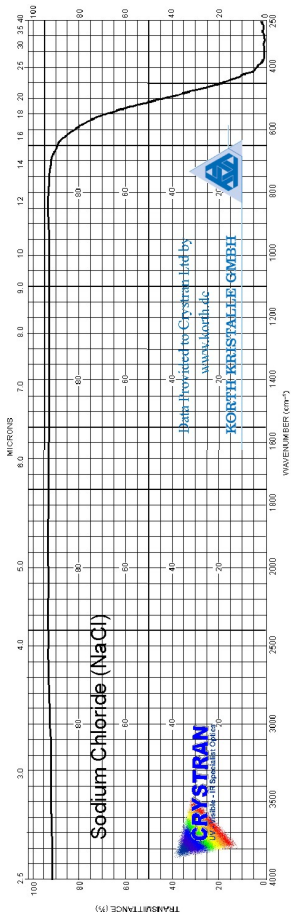

Figure A.1: Transmittance plot of sodium chloride, the data is gotten from www.crystran.co.uk (suppliers of the salt)

Appendix B

Labview PID controller

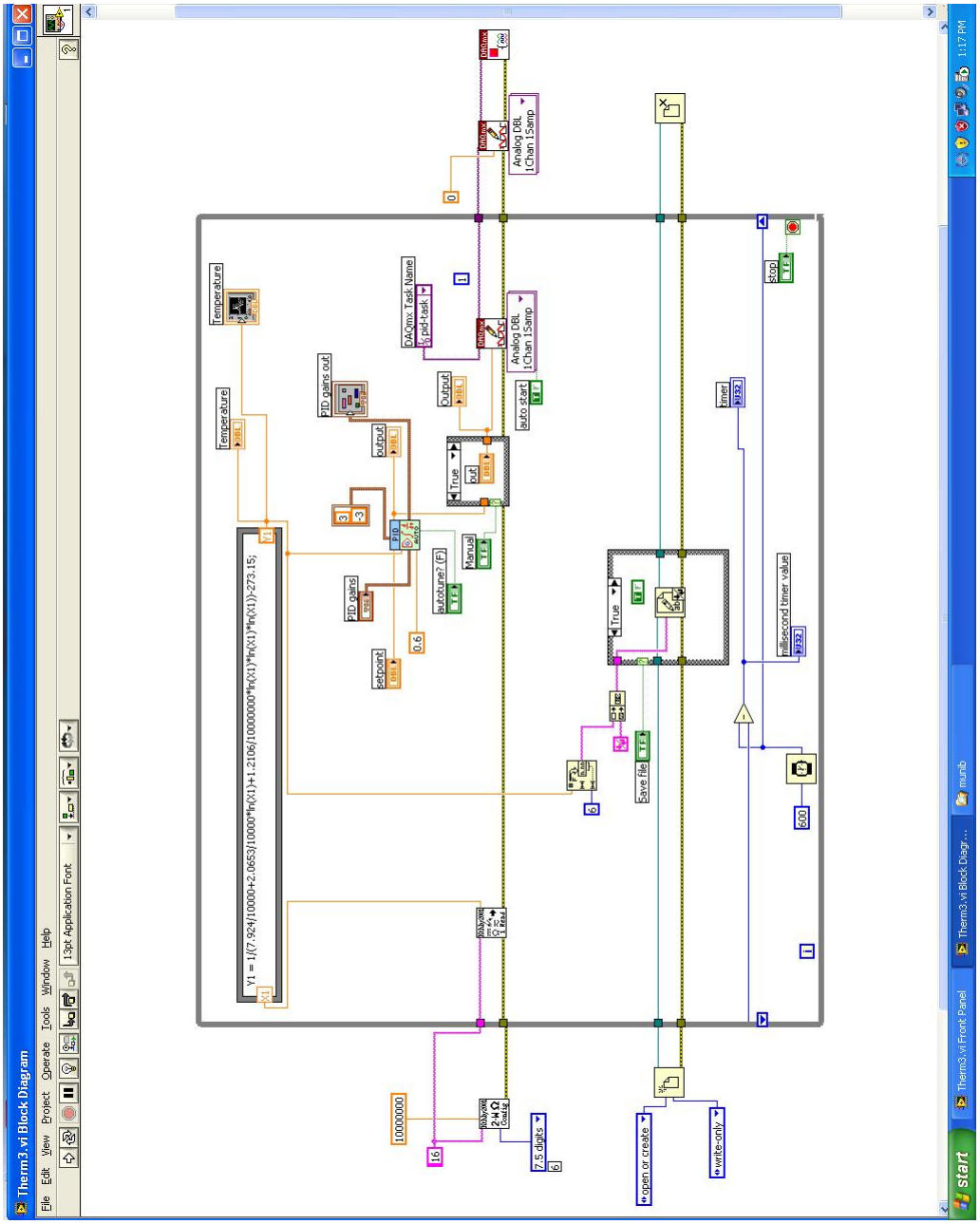

Figure B.1: A labview PID controller program for a thermistor.

Appendix C

Matlab code

```
clear

%physical constants
k0  =1.38065*10^-23;
hpl = 6.626069*10^-34;
Tstart = 283.15;
Tend   = 323.65;
Tdelta = 0.5;
light = 2.99792459*10^8;
A = 2*hpl*light^2;
B =hpl*light/k0;

% iteration steps
Temp = [Tstart:Tdelta:Tend];
delta_lamda = 1*10^-9;
lamda = [3*10^-6:delta_lamda:5*10^-6];
integrated  = zeros(length(Temp),1);

%integration loop
for j=1:length(Temp)
    % integrating in wavelength
    for i=1:length(lamda)
        energy(i)     = A/(lamda(i)^5*(exp(B/(lamda(i)*Temp(j)))-1));
       if i==1 || i==length(lamda)
        integrated(j) = integrated(j) + energy(i)*delta_lamda/2;
       else
        integrated(j) = integrated(j) + energy(i)*delta_lamda;
```

```
       end
    end
end


% loading images
for i=1:41
    s = ['nocor' int2str(i+9) '_50001'];
    Ab = load (s);
    img(:,:,2*i) = getfield(Ab,s);
    time(:,2*i) = getfield(Ab,[s ,'_DateTime']);
end
for i=1:41
    s = ['nocor' int2str(i+9) '0001'];
    Ab = load (s);
    img(:,:,2*i-1) = getfield(Ab,s);
    time(:,2*i-1) = getfield(Ab,[s ,'_DateTime']);
end
% building a time loop
num        = size(img,3);
time2      = diff(time,1,2);
time2(4,:) = time2(4,:)*3600;
time2(5,:) = time2(5,:)*60;
time2(6,:) = time2(6,:);
time2(7,:) = time2(7,:)/1000;
dt(2:num)  = sum(time2);
for j=2:num
    dt2(j)     = sum(dt(1:j));
end
% averaging over images
for j=1:num
    av_img(j,1) = mean(mean(img(:,:,j)));
end



% plotting the temperature against the IR data
figure(1)
plot(Temp,av_img,'-xk'),
xlabel('Temperature [K]','fontsize',14),ylabel('IR camera [S]','fontsize',14)
```

```
% plotting the intensity against the IR data
figure(2)
hold on
plot(integrated(2:end),av_img(2:end),'.k')
ylabel('IR camera [S]','fontsize',14),
 xlabel('Radiant excitance [J/(s*A)]','fontsize',14)
```

Bibliography

[1] *The Mechanics of Earthquakes and Faulting*, 2nd ed. Cambridge University Press, 2002.

[2] Bizzari, A., and Cocco, M. A thermal pressurization model for the spontaneous dynamic rupture propogation on a 3d fault. *Journal of geophysical research 111*, B05303 and B003864 (2006a-b).

[3] Bowden, F. P., and Thomas, P. H. The surface temperature of sliding surfaces. *Proc. Royal Soc. London A*, 223 (1954), 29–40.

[4] Brodsky, E. E., and Kanamori, H. Elastohydrodynamic lubrication of faults. *Journal of geophysical research 106*, 16,357-16,374 (2001).

[5] Chester, F. M., and Chester, J. S. Ultracataclastic structure and friction process of the punchbowl fault, san andreas system, california. *Techtonophysics 295* (1998), 199–221.

[6] Cooke, M. L., and Murphy, S. Assesing the work budget and efficiency of fault systems using mechanical models. *Journal of Geophysical reaserch 109*, B10408 (2004).

[7] Crank, J. *The Mathematics of Diffusion.* Oxford University Press, USA, 1980.

[8] Di Toro, G., D. L. G., and Tullis, T. E. Friction falls towards zero in quartz as slip velocity approaches seismic rates. *Nature*, 427 (2004), 436–439.

[9] Gaussorgues, G. *Infrared Thermography*, 3rd ed. Microwave technology series 5. Chapman and Hall, 1994.

[10] Goldsby, D. L., and Tullis, T. E. Low frictional strength of quartz rocks at subseismic slip rates. *Geophysical research letters 29*, 1844 (2002).

[11] Hirose, T., and Shimamoto, T. Growth of molten zone as a mechanism of slip weakening of simulated faults in gabroo during frictional melting. *Journal of geophysical research 110*, B05202 (2005).

[12] http://en.wikipedia.org.

[13] http://en.wikipedia.org/wiki/Halite.

[14] http://www.crystran.co.uk.

[15] http://www.egglescliffe.org.uk/physics /astronomy/blackbody/bbody.html.

[16] Kanamori, H. The diversity of the physics of earthquakes. *Proc. Jpn. Acad.*, B80 (2004).

[17] Kanamori, H., and Rivera, L. Energy partitioning during an earthquake. In *Earthquakes, Radiated Energy and the Physics of Faulting.* Geophysical Monograph Series 170, 2006, pp. 3–13.

[18] Kaufman, D. W. *Sodium Chloride.* American chemical society monograph. Reinhold Publ. New York, 1960.

[19] Lachenbruch, A. H. Frictional heating, fluid pressure, and the resistance to fault motion. *Journal of geophysical research 85*, B11 (November 1980), 6097–6112.

[20] Mair, K., and Renard, F. Thermal imaging on simulated faults during frictional sliding. *Geophysical reaserch letters 33*, L19301 (2006).

[21] Mase, C. W., and Smith, L. Pore-fluid pressures and frictional heating on a fault surface. *Pure Appl Geophys. 122* (1984/1985), 583–607.

[22] Mase, C. W., and Smith, L. Effects of frictional heating on thermal, hydrologic, and mechanical response of a fault. *Journal of geophysical research 92*, B7 (June 1987), 6249–6272.

[23] Michael L. Blanpied, T. E. T., and Weeks, J. D. Effects of slip, slip rate, and shear heating on the fricion of granite. *Journal of Geophysical reaserch 103*, B1 (2004), 489–511.

[24] Noda, H., and Shimamoto, T. Thermal pressurization and slip-weakening distance of a fault: An example of the hanaore fault, southwest japan. *Bull. Seis. Soc. Am. 95* (2005), 1224–1233.

[25] Rempel, A. W., and Rice, J. R. Thermal pressurization and melting in fault zone. *Journal of geophysical research*, B04314 (2006).

[26] Rice, J. R. Heating and weakening of faults during earthquake slip. *Journal of geophysical research 111*, B05311 (2006).

[27] S. M. Wiederhorn, R. L. M., and Bean, B. L. Plastic deformation and the fracture surface energy of sodium chloride. *Journal of the American Ceramic Society 53*, 1 (1970), 18–23.

[28] Schroeder, D. V. *An introduction to Thermal Physics.* Addison Wesley Longman, 2000.

[29] Sibson, H. R. Generation of pseudotachylyte by ancient seismic faulting. *Geophysical J. R. Astron. Soc. 43* (1975), 775–794.

[30] Sibson, R. H. Interactions between temperature and pore-fluid pressureduring earthquake faulting and a mechanism for partial or total stress relief. *Nature 243* (1973), 66–68.

[31] Sibson, R. H. Thickness of seismic slip zone. *Bull. Seis. Soc. Am. 93* (2003), 1169–1178.

[32] Siegel, R., and Howell, J. *Thermal radiation heat transfer*, 4 ed. Taylor and Francis, 2002.

[33] Tsatsumi, A., and Shimamoto, T. High-velocity frictional properties of gabroo. *Geophysical research letters 24*, 6 (March 1997), 699–702.

[34] Venkataraman, A., and Beroza, G. C. A brief review of techniques used to estimate radiated seismic energy. In *Earthquakes, Radiated Energy and the Physics of Faulting.* Geophysical Monograph Series 170, 2006, pp. 15–24.